Pinna-related transfer functions and lossless wave equation using finite-difference methods: Verification and asymptotic solution

Sebastian T. Prepeliţă[a)]

Department of Computer Science, Aalto University, Otaniementie 17, P.O. Box 15500, FI-00076 Aalto, Finland

Javier Gómez Bolaños[b)]

Department of Signal Processing and Acoustics, Aalto University, P.O. Box 13000, FI-00076 Aalto Espoo, Finland

Michele Geronazzo

Department of Architecture, Design, and Media Technology, Aalborg University, A. C. Meyers Vænge 15, 2450 København SV, Denmark

Ravish Mehra

Facebook Reality Labs, 8747 Willows Road, Redmond, Washington 98052, USA

Lauri Savioja

Department of Computer Science, Aalto University, Otaniementie 17, P.O. Box 15500, FI-00076 Aalto, Finland

A common approach when employing discrete mathematical models is to assess the reliability and credibility of the computation of interest through a process known as solution verification. Present-day computed head-related transfer functions (HRTFs) seem to lack robust and reliable assessments of the numerical errors embedded in the results which makes validation of wave-based models difficult. This process requires a good understanding of the involved sources of error which are systematically reviewed here. The current work aims to quantify the pinna-related high-frequency computational errors in the context of HRTFs and wave-based simulations with finite-difference models. As a prerequisite for solution verification, code verification assesses the reliability of the proposed implementation. In this paper, known and manufactured formal solutions are used and tailored for the wave equation and frequency-independent boundary conditions inside a rectangular room of uniform acoustic wall-impedance. Asymptotic estimates for pinna acoustics are predicted in the frequency domain based on regression models and a convergence study on sub-millimeter grids. Results show an increasing uncertainty with frequency and a significant frequency-dependent change among computations on different grids. © *2019 Author(s). All article content, except where otherwise noted, is licensed under a Creative Commons Attribution (CC BY) license (http://creativecommons.org/licenses/by/4.0/).* https://doi.org/10.1121/1.5131245

I. INTRODUCTION

The head-related transfer functions (HRTFs) represent the acoustical paths from a stationary sound source to the ears of the listener under free field conditions, encoding the anatomical filtering effects which embed the auditory cues used for localizing sound sources.

Unless cue remapping occurs,[1] HRTFs are usually not perceptually transferable.[2] This is mainly due to the high degree of personalization of the human pinna.[3] Currently, the main two methods for obtaining an estimate of individualized HRTFs are measurements and simulations. Measurements are the traditional method, based on which HRTFs were perceptually validated.[4–7] Although HRTF measurements can nowadays be done within a relatively short time,[8–10] they are still, in many ways, impractical: high accuracy could be challenging, specialized equipment prevents scalability, while subjects undergo a generally tedious measurement session.

Wave-based numerical simulations are an alternative which could eventually offer greater flexibility when compared to measurements. Presently, the boundary element method (BEM)[11–15] and the finite difference time domain (FDTD)[16–18] methods are the most common HRTF simulation methods. Despite the many attractive properties of the HRTF numerical simulations, their validity and reliability in the full audible frequency bandwidth has not yet been established using strong validation studies as those defined in the verification and validation (V&V) literature.[19,20] Moreover, studies of numerical sensitivity/uncertainty analysis involving HRTF simulations are also scarce.[18,21]

[a)]Electronic mail: sebastian.prepelita@aalto.fi
[b)]Current address: Hefio Ltd., Otakaari 5 A, 02150 Espoo, Finland.

The most challenging HRTF phenomena to be simulated are the pinna effects which occur above 3 kHz.[22] The pinna-related transfer function (PRTF) provides the isolated information of the pinna acoustics and can be used to focus the analysis to such a challenging problem.

Any computation will contain approximations and specific errors which could render the result unreliable. Present HRTF computations seem to lack a strong formal assessment of reliability and credibility of the computed solutions. Consequently, it not only becomes difficult to assess the predictive quality of the wave-based model employed, but also wrong conclusions could be reached. The present study aims to quantify the quality of computed wave-based PRTF/HRTF solutions with focus on FDTD methods. Formal solutions and their precision are estimated by asymptotically extrapolating the results from computations on multiple sub-millimeter grids. In turn, the uncertainty between HRTF measurements and simulations can be quantified to the complementary benefit of both approaches.[23]

This work is the first part of a comprehensive V&V study. Validation with measurements of the present PRTF results will be part of a separate validation study.

II. BACKGROUND

Linear acoustics is described by a linear and well-posed continuous problem (in the Hadamard sense). Thus, any consistent and stable approximation will theoretically converge to the same solution (invoking the Lax-Richtmyer equivalence theorem), independent of the mathematical formulation of the continuous model and of the discrete model employed (e.g., BEM, FDTD). Depending on the formulation and properties of the continuous solution, any computational implementation and execution will involve model-specific deviations from the formal behavior. In practice, such computational errors could interact in a complex manner thus requiring empirical reliability assessment of the final computations.

Here, a simple explicit and stable[24] finite-difference method is chosen which is amenable to parallelization. Its simplicity and extensive study facilitates the understanding of various error sources present in a final computation. Moreover, the finite-difference literature is extensive and offers formal methods/models to study the usually-dominant (Ref. 20, p. 286) discretization error. Such methods can be transferred from other fields and advantageously employed to empirically estimate the quality of the computations, given the complex PRTF problem at hand.

A. PRTFs

The PRTFs are formally defined in the frequency domain as the following transfer function:

$$\text{PRTF}(\mathbf{r}_1, \Omega) = \frac{P_{\text{ear}}(\mathbf{r}_1, \Omega)}{P_{\text{ref}}(\mathbf{r}_1, \Omega)}, \tag{1}$$

where $\mathbf{r}_1 \in \mathbb{R}^3$ denotes the continuous location of the source, $P_{\text{ear}}(\Omega)$ represents the Fourier transform of the captured pressure at a fixed location of interest inside a pinna

cavity, and $P_{\text{ref}}(\Omega)$ is the Fourier transform of a recorded pressure with the pinna absent.

B. Continuous model

As partial differential equation (PDE), the inhomogeneous scalar wave equation (Ref. 25, p. 162) is considered which can be written in some continuous three-dimensional (3D) domain $\mathcal{D}$ as

$$\frac{\partial^2 p(\mathbf{r}, t)}{\partial t^2} = c^2 \mathbf{V}^2 p(\mathbf{r}, t) + f(\mathbf{r}, t), \tag{2}$$

where $\mathbf{r} = [x, y, z]^T \in \mathcal{D}$ (with $\mathcal{D} \subseteq \mathbb{R}^3$), t represents time, $\nabla = [(\partial/\partial x), (\partial/\partial y), (\partial/\partial z)]$ represents the 3D Cartesian del differential operator, c is the sound speed, $p : \mathbb{R}^3 \times \mathbb{R}_+ \rightarrow \mathbb{R}$ is the scalar pressure field, and $f : \mathbb{R}^3 \times \mathbb{R}_+ \rightarrow \mathbb{R}$ is a general analytical forcing or driving function. c is assumed constant in the homogeneous and quiescent medium within $\mathcal{D}$.

At the boundary surface(s) $\partial \mathcal{D}$, the following frequency-independent resistive boundary condition (BC) of local reaction is employed for the pressure field:

$$-\mathbf{n} \cdot \mathbf{V} p(\mathbf{r}_b, t) = \frac{\beta(\mathbf{r}_b)}{c} \frac{\partial p(\mathbf{r}_b, t)}{\partial t}, \tag{3}$$

where $\mathbf{n}$ represents the outward (pointing, locally, from $\mathcal{D}$ into any solid in contact with $\mathcal{D}$) normal to the surface boundary at point $\mathbf{r}_b \in \partial \mathcal{D}$, and β is the specific acoustic admittance at the boundary (Ref. 26, p. 261), see the derivation in, e.g., the work by Kowalczyk and van Walstijn.[27]

C. Discrete models

In this study, an FDTD mathematical model is used to discretize Eq. (2). Rigorously, the update discretizes the integral form of Eq. (2), however for the uniform Cartesian grid used, the discretization of the strong form in Eq. (2) is found[24] for the interior update.

The second-order accurate standard rectilinear (SRL) explicit update is obtained on the interior and employed on a cubic Cartesian grid with voxel size of ΔX. A frequency independent impedance can be set for the locally reacting stair-cased boundaries using an "upwind" approximation for the pressure field at the boundary.[28] The code supports three types of sources: *soft*, *hard*, and *transparent*.[29] The explicit FDTD update can be derived using finite volume (FV) methods[24] and can compactly be written for pressure and a soft source as

$$P_i^{n+1} \left[1 + N_i \lambda_{\mathcal{C}} \frac{\beta_i}{2} \right] = \lambda_{\mathcal{C}}^2 \sum_{j=1}^{6-N_i} \left[P_j^n - P_i^n \right] + 2 P_i^n$$
$$- P_i^{n-1} \left[1 - N_i \lambda_{\mathcal{C}} \frac{\beta_i}{2} \right] + \Delta T^2 F_i^n, \tag{4}$$

where P_i represents the discretized pressure field at the 3D Cartesian index i, j indexes the neighboring air voxels for P_i, $\lambda_{\mathcal{C}} = c \Delta T / \Delta X$ is the Courant number (c is the sound speed), $N_i \in \{0, 1, 2, ..., 6\}$ represents the total number of solid (i.e., boundary) voxels adjacent to P_i [for $N_i = 6$ the sum in Eq. (4) is assumed to be 0], and F_i represents the local forcing

applied at the center of voxel i. In Eq. (4), for computer memory considerations, a unique specific acoustic admittance β_i is assumed for all boundary surfaces of each voxel i.

For simplicity and unambiguous definition of the grid spacing ΔX, the boundaries are discretized on the same uniform 3D Cartesian grid resulting in stair-stepped boundaries which are obtained from the mesh by using a voxelization algorithm. The adopted voxelization algorithm is the *conservative*[30] one since, although not ideal, it is well-defined and convenient to use.

1. Distributed computing model

The simulation domain was split against the Cartesian z axis: $\mathcal{D}$ is partitioned in *domains* distributed across computing nodes, while each domain is partitioned in *subdomains* across Graphics Processing Unit (GPU) devices available at each compute node. See more details about the implementation in Appendix B.

To avoid extra difficulties for a potential validation study such as convergence rates and correspondence with reality, the PRTF domain will be chosen without a commonly-employed perfectly matched layer absorbing bounding boundary. Consequently, the PRTF domain size is scaled such that no reflection from the room walls arrives at the receiver locations.

D. Simulation errors

Depending on modeling and computational choices, there are multiple sources of error,[31] which could coexist in a simulated result and affect the computations. Such errors make it highly unlikely that the formal (i.e., asymptotic, as $\Delta X \to 0$) solution is computed in practice: given a discrete model and its computational implementation, the discrete solution will at best be within a ball $\mathcal{B}(p(\mathbf{r},t),\varepsilon)$ of radius ε proportional to the machine epsilon away from the unique formal solution $p(\mathbf{r},t)$. As such, it is useful to identify and understand the behavior of the main sources of error for the model and problem at hand, also considering that error cancellation could occur (Ref. 20, p. 382) in a computation when multiple sources of error are present, together with other unacknowledged[23] errors.

Table I summarizes the following sources of error:

Discretization error is caused by the approximation of the continuous operators in the employed PDE in Eqs. (2) and (3) by discrete operators.

A first-order truncation error is found for the BC which propagates over interior solutions (Ref. 33, p. 159). For example, the local truncation error for a velocity v_b used in the flux at a boundary orthogonal to the x axis is

TABLE I. Relevant sources of error for the employed discrete models and problem of interest, relative to the formal solution of the PDE model in Eqs. (2) and (3) assuming the triangulated mesh as the true geometry.

Discrete model error	Cause	General behavior	*A priori*/formal order		Comments
			Time	Space	
Discretization	Approximation of continuous differential operators	• Increases with frequency (scheme-dependent) • Direction dependent	$O(\Delta T^2)$	$O(\Delta X)$	At an absorbing boundary ($\beta > 0$)
		• Increases with simulated time • Depends on $\lambda_{\mathcal{C}}$	$O(\Delta T^2)$	*exact*	At a voxelized rigid boundary
		• Depends on the formal solution	$O(\Delta T^2)$	$O(\Delta X^2)$	For the interior update
Round-off	Finite-precision representation of numbers	• Dominates the lower frequency range • Usually increases with simulated time • Depends on implementation	$O(\Delta T^{-1})$	$O(\Delta X^{-3})$	Seen in the $\Delta X \to 0$ limit as[a] $O(\Delta X^{-4})$ in an FDTD simulation of Eq. (2)
Pollution	Accelerated growth with frequency in HOT of the discretization error	• Increases with frequency		Lowers the observed order of discretization error	Also "caused" by spectral inconsistencies of initial conditions
Voxelization	Stair-step representation of the boundary	• Increases with frequency • Depends on geometry, voxelization algorithm (Ref. 18), mesh alignment and orientation, wave incident angle (Ref. 32), grid origin, update scheme		$O(\Delta X)$	For distances Surfaces might not converge
		• Might not preserve relevant topological features		$O(\Delta X^3)$	For volumes
Interpolation	Space/time inconsistencies of computed/ injected field values	• Usually grows with frequency (depends on algorithm)	N/A[b]	$O(\Delta X)$	No interpolation (i.e., nearest neighbor)
			N/A[b]	$O(\Delta X^2)$	Trilinear interpolation

[a]Results obtained by applying *a priori* bounds (Ref. 36) within a multiplicative separation of variables frame (Ref. 34) coupled with the ordering $\Delta X^{-j} \ll \Delta X^{-(j+1)}$ as $\Delta X \to 0$ with $j \in \mathbb{N}^*$.

[b]Due to the frequency division in Eq. (1) and the frequency-analysis for computed PRTFs, temporal interpolation is not considered (N/A) in the present work. See more details in the text, Sec. II D.

J. Acoust. Soc. Am. **146** (5), November 2019

Prepeliţă et al.   3631

$$v_b(t) - \beta_b P_j(t) = \beta_b \frac{\Delta X}{2} \frac{\partial p_b(t)}{\partial x} + \beta_b \cdot \text{HOT}(t), \quad (5)$$

where p_b is the pressure at the boundary surface b, P_j is the pressure at the center of a neighboring voxel j, β_b is the specific acoustic admittance at b, and HOT stands for[19] "higher order terms" in ΔX.

Analysis of the *global* discretization error is generally making use of a series expansion of the truncation error. For the employed scheme and temporarily ignoring the initial conditions and the boundary modeling, as $\Delta X, \Delta T \rightarrow 0$, an FDTD-simulated pressure $\widetilde{p}_{\mathbf{r}_1}(t)$ at $\mathbf{r} = \mathbf{r}_1 \in \mathbb{R}^3$ can be expressed as (Ref. 33, p. 217)

$$\begin{aligned}\widetilde{p}_{\mathbf{r}_1}(t, \Delta T, \Delta X) = {}& p_{\mathbf{r}_1}(t) + \epsilon_{t,\mathbf{r}_1}(t)\Delta T^2 \\ & + \epsilon_{x,\mathbf{r}_1}(t)\Delta X^q + \text{HOT}(t), \end{aligned} \quad (6)$$

where $p_{\mathbf{r}_1}(t)$ is the asymptotic solution; $\epsilon_{t,\mathbf{r}_1}(t)$ and $\epsilon_{x,\mathbf{r}_1}(t)$ are the *principal* (Ref. 33, p. 158) temporal and spatial error terms, respectively, q is the leading spatial formal accuracy which can either be 2 for rigid boundaries or 1 for absorbing boundaries close enough to $\mathbf{r}_1$; and $\text{HOT} = O(\Delta T^4, \Delta X^{2q})$. For fixed $\mathbf{r}_1$, $\epsilon_{t,\mathbf{r}_1}(t)$ satisfies a differential equation that depends on the update and $p_{\mathbf{r}_1}(t)$ (see, e.g., Secs. III 9 and III 10 in Hairer *et al.*[33]) while the temporal dependence of $\epsilon_{x,\mathbf{r}_1}(t)$ is given by $p_{\mathbf{r}_1}(t)$.[34] Thus, even a discrete delta sequence can be used as the excitation signal without aliasing of the discrete-time Fourier transform (DTFT) of the error terms $\mathcal{E}_{t/x}(\omega) = \text{DTFT}\{\epsilon_{t/x}(t)\}$ and $\text{HOT}(\omega)$ in Eq. (6).

Asymptotic range is attained when the deviation of the discrete solution from the formal solution behaves according to the expected leading[19,35] space and/or time truncation error terms. In the following, it is assumed the discrete solutions are stepped at stable values of λ_C with negligible global interactions (e.g., cancellation) between the spatial and temporal truncation errors.

Round-off errors emerge due to the finite precision representation of numbers in the FDTD solver. *A priori* analysis shows divergence of results: assuming an additive round-off error, a theoretical $O(1/\Delta X)$ behavior is found for an ordinary differential equation (see, e.g., May and Noye[36]). In practice, the behavior of the round-off error is less understood.[37]

Initial conditions could affect both the convergence rates and the magnitude of the error terms (see, e.g., Chap. 10 in the work by Strikwerda[38]). Here, two main aspects are of interest: (i) spectrum inconsistencies [e.g., a discrete delta has a continuous temporal gain of $O(\Delta T)$ and spatial gain[39] of $O(\Delta X^3)$]; and (ii) the *pollution error*[40] [e.g., the local principal spatial error grows as (Ref. 84, p. 5) $O(\omega^4 \Delta X^2)$]. The latter is avoided by using "smooth enough" (i.e., low-passed) sampled initial conditions.[41]

Boundary modeling errors are related to the non-trivial grid-generation problem and emerge here due to the voxelized boundary surface $\widetilde{\partial \mathcal{D}}(\Delta X)$. The voxelization process will induce:

(1) a volume convergence of $O(\Delta X^3)$;
(2) a first-order[42,43] distance convergence non-parallel to the boundary $\partial \mathcal{D}$ behaving as $O(\omega \Delta X)$;[44]

(3) spurious local "excess scattering"[45] of high-frequency waves that basically pollute the solution; and
(4) unlikely convergence of the voxelized surface area[46] $\widetilde{\partial \mathcal{D}}(\Delta X)$ for a complex geometry such as a human pinna.

Such errors are scheme-dependent,[47] generally converge non-smoothly in ΔX, and could negatively impact the observed convergence rates even below first-order.[48,49]

Location-related inconsistencies will cause a first-order error due to source/receiver locations at voxel centers. For a point source/receiver (Ref. 19, p. 173) in the FV interpretation of the scheme,[50] an unpractical odd grid refinement ratio $\mathfrak{r} = \Delta X_{\text{old}}/\Delta X_{\text{new}}$ of $\mathfrak{r} = 2k+1$ with $k \in \mathbb{N}^*$ would be required. Alternatively, distributed sources/receivers could be employed, or interpolation used as post-processing.

III. METHODS

Verification procedures are broadly concerned with the precision and/or accuracy of actual computations.[23] In the V&V literature, they involve two main procedures:

- *code verification*: assesses whether the computational model is a faithful implementation of the discrete mathematical model;[23]
- *solution verification*: assesses the accuracy, relative to the formal solution, of computed solutions by the/a previously verified computational model.

Both procedures imply empirically studying how refining the grid (i.e., ΔX, ΔT) affects the computed solutions.

The formal (*time*, *space*) order of accuracy of the scheme will initially be denoted by (g, q). More details on mathematical notation can be found in Appendix A.

A. Code verification

The order of accuracy test is usually considered the most difficult to satisfy code verification procedure for PDE simulations.[35] It involves comparing the observed order of accuracy (i.e., the rate by which the discretization error empirically decreases with ΔX) with the formal order of the employed scheme (i.e., the expected rate of decrease in error with ΔX emerging from a truncation error analysis). This is usually[19,35,51] achieved by comparing computations against band- and energy-limited continuous solutions: (i) simple *exact solutions* (ESs) or (ii) *manufactured solutions* (MSs) (i.e., solutions which do not satisfy the given PDE).

To avoid voxelization errors (see Sec. II D), the utilized continuous solutions are chosen inside an axis-aligned rectangular room of dimensions $[L_x, L_y, L_z]^T$ with uniform admittance on all the walls.

For the comparison with the analytic solutions, the discretized $l_{\Delta X}^2$-norm is used to compute the global error

$$\|\epsilon\|_2 = \sqrt{\Delta V \sum_{m=0}^{N-1} \left(P_m^{t_n} - p(\mathbf{M}, t_n)\right)^2}, \quad (7)$$

where $N = N_x N_y N_z$, $\Delta V = (\Delta X)^3$, m indexes all the voxels residing in the interior air volume $\Delta X \cdot [0, N_x) \times [0, N_y) \times [0, N_z)$, $L_{x/y/z} = N_{x/y/z} \Delta X$, $\mathbf{M} = \Delta X [i + 0.5, j + 0.5, k + 0.5]^T$, $P_m^{t_n}$ is the computed pressure field at time $t_n = n\Delta T = t_{sim}$, and p is the manufactured or ES.

The initial conditions are used to drive the simulations and are applied at all points $\mathbf{M}$ of the interior air volume and are set based on the continuous solutions: $p(\mathbf{M}, 0)$ and $p(\mathbf{M}, \Delta T)$. For the MS, the forcing terms are implemented as *soft* sources and are evaluated in the center of the voxels from $2\Delta T$ onwards. See more details in Appendix B.

1. ES

To avoid possible difficulties (Ref. 19, p. 82) arising from using existing power series solutions in rectangular rooms,[52,53] a first simple approach to code verification is to assume the walls are perfectly reflecting for which an eigenvalue solution exists (Ref. 26, p. 571). The ES was chosen as the following closed-form eigenfunction:

$$p_{ES}(\mathbf{r}, t) = P_0 \cos(\Omega_n t) \cos\left(\frac{\pi d_x}{L_x} x\right)$$
$$\times \cos\left(\frac{\pi d_y}{L_y} y\right) \cos\left(\frac{\pi d_z}{L_z} z\right), \tag{8}$$

where $d_{x/y/z} \in \mathbb{Z}$ and $\Omega_n^2 = c^2 \pi^2 [(d_x/L_x)^2 + (d_y/L_y)^2 + (d_z/L_z)^2]$. No analytic forcing term exists for the ES [i.e., $f_{ES}(\mathbf{r}, t) = 0$].

2. MS

Although rigid-wall PRTF computations are assessed in the present work, results of code verification for various boundary impedance values are presented to (i) have full code verification coverage for the solver, and (ii) examine a toy problem in which multiple sources of error having different asymptotic behaviors are present.

A solution is manufactured inside a rectangular room for $\beta \neq 0$. The method of MSs solves the PDE problem backwards;[51] the forcing term in Eq. (2) is determined by applying the differential operators of the PDE from Eq. (2) to the *a priori* chosen solution. Moreover, to test the boundary update, the MS should satisfy the BCs. The MS is chosen in the form

$$p_{MS}(\mathbf{r}, t) = P_0 e^{-k_d t} \cos(k_x x + \phi_x) \cos(k_y y + \phi_y)$$
$$\times \cos(k_z z + \phi_z), \tag{9}$$

where $P_0 \in \mathbb{R}$ represents the amplitude, $k_d \in \mathbb{R}$ can be viewed as the "decay"[53] or "attenuation"[52] constant, $k_{x/y/z} \in \mathbb{R}$ is the Cartesian components of the wavenumber, and $\phi_{x/y/z} \in \mathbb{R}$ are the phase components of the spatial modes. If the BCs are satisfied, then

$$k_{x/y/z} = \frac{\pi d_{x/y/z} - 2\phi_{x/y/z}}{L_{x/y/z}}, \tag{10a}$$

$$k_d = \frac{c}{\beta} k_{x/y/z} \tan(\phi_{x/y/z}), \tag{10b}$$

where $d_{x/y/z} \in \mathbb{Z}$ and a uniform β is assumed for all walls. For the chosen MS to satisfy both Eqs. (10a) and (10b), only some combinations of $L_{x/y/z}$, $\phi_{x/y/z}$ and $d_{x/y/z}$ are possible. By replacement in the wave Eq. (2), the MS from Eq. (9) yields an analytic forcing term

$$f_{MS}(\mathbf{r}, t) = \left[k_d^2 + c^2(k_x^2 + k_y^2 + k_z^2)\right] p_{MS}(\mathbf{r}, t). \tag{11}$$

Boundaries and interior test case. Here, the initial conditions are set for all grid points based on Eq. (9), while the discrete forcing terms are calculated based on Eqs. (4) and (11).

Interior test case. The code verification program is also error prone especially for the MS, for example, if any of the continuous functions are evaluated at an incorrect time sample, the error becomes proportional to ΔT, yielding a first-order observed accuracy. Consequently, the code verification is generally divided into more manageable tests: a second-order accuracy is expected for the MS if the code update is not exercised near the boundary voxels. To achieve this, a Dirichlet BC is usually used[51] at the edges of the domain—here, a *hard* source was employed instead of the soft source at each boundary voxel $\mathbf{m}_b$ surrounding the interior domain. Such source imposes a pressure field which is evaluated from the MS $p_{MS}(\mathbf{M}_b, t_n)$. For this scenario, the $l_{\Delta X}^2$-norm in Eq. (7) is restricted to the $\Delta X \cdot [1, N_x - 1] \times [1, N_y - 1] \times [1, N_z - 1]$ volume.

3. Simulations

To further simplify the problem, a cubic room is considered (i.e., $L_{x/y/z} = L$) together with $d_{x/y/z} = d$ for both the manufactured and ESs. In addition, $\phi_{x/y/z} = \pi/4$ is chosen for the MS.

To keep the observed error within an asymptotic range and within reasonable values relative to single precision, d is fixed at 1, $\lambda_C = 0.5$, $P_0 = 1$, $c = 340$ [m/s], while $L = 1.28$ [m]. In addition, the grid is halved (at constant λ_C and c) starting from $\Delta X_{max} = 0.16$ [m] yielding the coarsest interior grid having $N_{x/y/z} = 8$ voxels per Cartesian dimension. The grid spacing used in the refinement study is: $\Delta X \in \{16, 8, 4, 2, 1\}$ [cm]. The cubic room mesh was specifically designed for the used grids with double walls such that the voxelized domain $\mathcal{D}$ remains consistent between grids.

The grid halving is also convenient since the error can be evaluated at exactly the same time t_{sim}: the number of time samples N_t doubles by each halving of the grid for fixed λ_c and c. Thus, no temporal interpolation is needed. Initial conditions excite the code-verification simulations which are initialized at $t = 0$ and $t = \Delta T$ from the formal solution and ran until a fixed time $t_{sim} \approx 6.59$ [ms]. t_{sim} is chosen such that it is divided by the coarsest sampling time $t_{sim} = N_t \Delta T_{max}$ with $N_t \in \mathbb{N}^*$ and such that it is of similar order with PRTF simulation times (see Sec. III B 5). The final number of time steps including the two initial conditions is $N_t \in \{28, 56, 112, 224, 448\}$ [steps], since the initial conditions were given as input, $N_t - 1$ steps are actually computed for each grid.

Large-scale and distributed simulations could present additional challenges. In the present framework, a reasonable Message Passing Interface (MPI) code verification
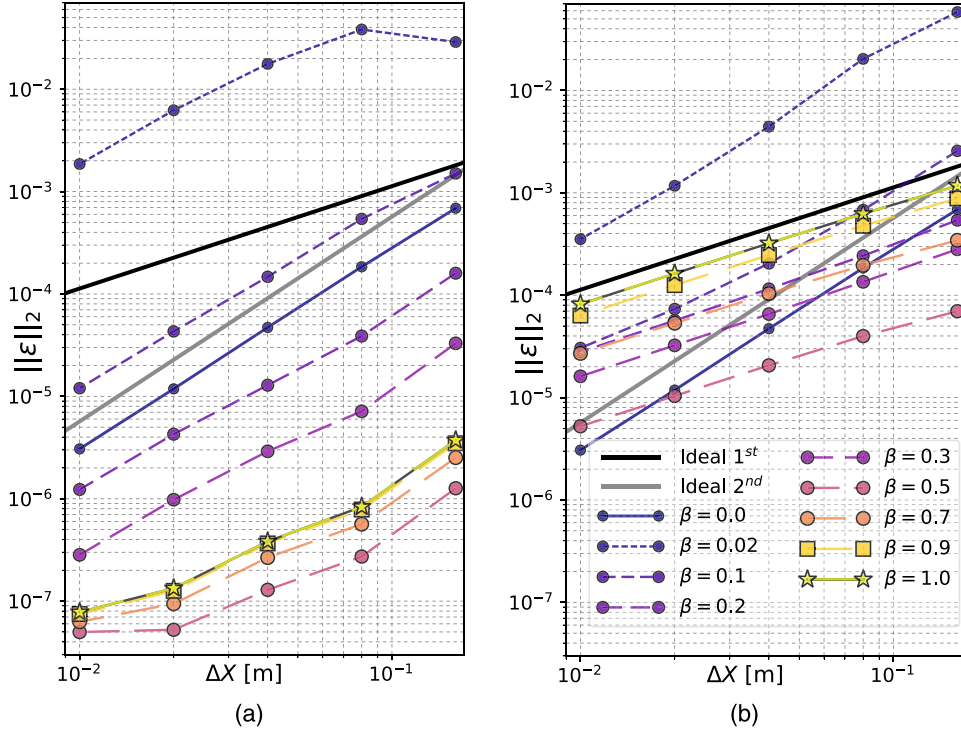
J. Acoust. Soc. Am. **146** (5), November 2019

Prepeliţă *et al.* 3633

FIG. 1. (Color online) Observed global spatial $l^2_{\Delta X}$ error norm $||\epsilon||_2$ at $t = 6.59$ [ms]. $L = 1.28$ [m], $P_0 = 1$, $\lambda_C = 0.5$, [1,1,1] mode, 3 MPI nodes. The line for a zero specific acoustic boundary admittance β correspond to the ES case [i.e., rigid box in Eq. (8)] while the other lines are for the MS in Eq. (9). The slopes give the convergence rates: the solid black and gray lines are shown as visual anchors for a first- and second-order error convergence, respectively. (a) Interior and (b) boundary.

should satisfy the following aspects: (i) each type of partition (e.g., bottom, middle, top) in the MPI-partitioning configuration will be part of the simulation and (ii) the FDTD update CUDA kernel is exercised in each domain and subdomain. Here, the former condition is satisfied when at least three MPI nodes are entailed in the code verification procedure; for the latter, each subdomain must contain at least two z-slices (due to the implementation).

For large values of ΔX, not all simulations can be computed utilizing all the available devices per MPI node. As such, for each node the number of utilized devices is lowered prior to the domain partitioning such that a subdomain of two z-slices is assigned to each of the utilized devices. For example, each utilized node contained 16 available GPU devices which meant the following number of devices per node was used: $\{2, 3, 7, 13, 16\}$ [nodes] corresponding to $\Delta X \in \{16, 8, 4, 2, 1\}$ [cm].

The code verification program has four main inputs:

(1) a list of grid spacings;
(2) the number of MPI nodes;
(3) the number of utilized GPU devices per node;
(4) a triangulated mesh geometry that represents the described cubic room which is further voxelized for each grid spacing ΔX_i.

Consequently, the MPI domain and subdomain partitioning together with the voxelization process are also tested to some small extent during code verification.

4. Code verification results and discussion

The observed errors are shown in Figs. 1(a) and 1(b). Table II displays q_{obs} from an ordinary least squares fit on the error curves in Fig. 1 based on the $||\epsilon||_2 = \epsilon_p \Delta X^{q_{obs}}$ regression model—linearized using the logarithm function.

As expected, the results for the ES are very close to second-order. A similar, yet not so clear, trend is seen in Fig. 1(a) for the MS and hard sources on the edges of the domain (second test case in Sec. III A 2) which provides evidence for the correctness of the code verification procedure. When the boundary update is also tested for the MS scenario (first test case in Sec. III A 2), the observed order of accuracy generally drops to first-order.

Figure 1(b) also shows that the discretization error introduced at the domain boundary can be weak enough at t_{sim}: for small values of β and certain grid spacings, the second-order principal error term from the interior update dominates the global error and the observed order of accuracy is 2. As such (in this case, smooth) transitions between different sources of error which have different smooth asymptotic behavior could be observed at some t_{sim} and for a range of ΔX, as one source of error starts dominating over the others.

TABLE II. Ordinary least squares fit on the error curves in Fig. 1. β represents the specific acoustic admittance, while R^2 is the coefficient of determination rounded to three decimal places.

MS $\beta \neq 0$ (Interior)			MS $\beta \neq 0$ (Boundary)		
β	q_{obs}	R^2	β	q_{obs}	R^2
0.02	1.05	0.864	0.02	1.89	0.997
0.1	1.76	0.999	0.1	1.60	0.993
0.2	1.72	0.998	0.2	1.07	0.999
0.3	1.66	0.994	0.3	1.03	1.000
0.5	1.17	0.914	0.5	0.94	0.998
0.7	1.32	0.964	0.7	0.92	0.999
0.9	1.37	0.974	0.9	0.95	1.000
1.0	1.38	0.974	1.0	0.96	1.000
ES $\beta = 0$					
β	q_{obs}	R^2			
0.0	1.96	1.000			

Finally, it can also be seen in Fig. 1(a) that the round-off error starts predominating for $\Delta X \leq 2.0$ [cm] and certain β values: the convergence rate appears to change to zero-order when the (global) error reaches a value around 0.5×10^{-7}, close to the machine epsilon of single precision for $P_0 = 1$.

The proposed code verification has some limitations. Ideally, the implementation of the voxelization process should be assessed independently of the discretization error through relevant $\partial\mathcal{D}$-related convergence studies. The authors are unaware of rigorous procedures to do so. Moreover, the present code verification exercise did not include the interpolation algorithms but their results were cross-checked against default software packages. Finally, the calculation of the $l_{\Delta X}^2$ norms is based on the full interior-pressure domain which is retrieved from the GPU memory at the end of each simulation. Consequently, the code for individual receivers was not considered. Nevertheless, such code involves simple memory transfers at each time step.

In summary, our results show that the utilized code behaves as expected and could be used for *a posteriori* error quantification. Although code verification cannot be complete,[23] the current results are considered satisfactory because the implementation of the FDTD update code, the initial conditions, two types of sources, the domain partitioning, and the MPI communication were assessed.

B. Solution verification of PRTF simulations

Solution verification is concerned with the assessment of numerical reliability of a computed solution: since asymptotic solutions are neither known for general problems nor can easily be computed in practice (see Sec. II D), the accuracy and/or precision of the result relative to the formal solution needs to be quantified.

Solution verification usually entails an *a posteriori* quantification of the dominant error for a particular computation. Most common in PDE problems, a technique based on Richardson extrapolation is used (Ref. 20, p. 284). This technique is reliably applied when the computed solution is in the asymptotic range. Thus, the asymptotic range of the computed PRTFs needs to be assessed such that the proper error estimate is used.

1. Source/receiver interpolation

To avoid location-induced errors (see Sec. II D), for each grid ΔX_i, second-order accurate trilinear interpolation is used at each simulated temporal sample and calculated using a tensor product of three linear Lagrange univariate interpolants.[54]

Subsequent to the receiver interpolation, the principle of reciprocity is re-invoked: each simulation can now be viewed as having the source at an interpolated location and the receiver at the center of an air voxel $\mathbf{r}_s$. Running multiple simulations with different source locations displaced relative to $\mathbf{r}_s$ by $\mathbf{m}\,\Delta X$ with $\mathbf{m} \in \mathbb{Z}^3$, the source location can thus be interpolated to a desired continuous location.

To facilitate the described interpolation and to minimize the number of simulations, the continuous interpolated source location $\mathbf{r}_{ear}$ was chosen as the center of the source

voxel on the grid on which the source was furthest from the input surface $\partial\mathcal{D}$. Farther was quantified in the outward direction on an imaginary "inter-aural" axis.

Due to the frequency-domain behavior of the used interpolant,[55] the monotonic increase with frequency in discretization error is expected to be preserved.
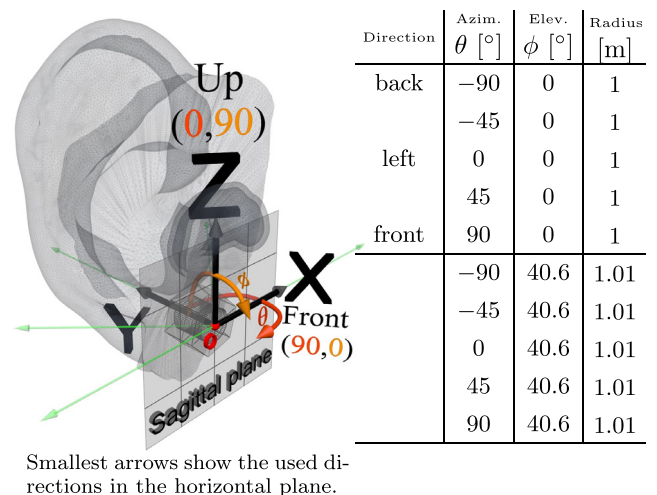
2. 3D pinna and PRTF simulation domain

The employed pinna mesh is a triangulated scan of a cast done on an otologically normal living human. The focus of this study is the blocked-meatus PRTFs. Consequently, an ear-blocking was designed to rigidly fit inside the ear canal and encapsulate a miniature microphone. In the present simulations, the microphone is replaced by a cylinder.

The origin O of the PRTF coordinate system was chosen along the axis of an M8 nut, in the back plane of the nut which is considered a sagittal plane (see Fig. 2 for more details). The central axis of the bolt was defined to be parallel to the interaural y axis. The *up* axis was chosen as the Cartesian z-axis yielding the x axis as the *front* direction.

For the ear simulation P_{ear} in Eq. (1), the pinna, the ear-blocking, and the nut meshes were placed inside a domain bounding-box which was chosen such that no reflections would reach the receiver locations during a considered time window of 6.25 [ms]. The corresponding direction-of-arrivals are given as (θ,ϕ) pairs with $\theta \in [-90°, 90°]$ and $\phi \in [-90°, 90°]$ representing azimuth and elevation angles, respectively (see Fig. 2). The reference simulation to estimate P_{ref} in Eq. (1) only contained the bounding-box and the source was placed and interpolated at a location close to the origin of the pinna coordinate system—see Sec. III B 1.

In Secs. III B 3 and III B 4, the PRTFs are computed using the principle of reciprocity (Ref. 25, p. 197) with the source at the blocked meatus location $\mathbf{r}_{ear}$ and at $\mathbf{r}_{ref} \equiv O$ with the ear absent. As such, the receivers will be placed at a point in the far-field $\mathbf{r}_1$ relative to $\mathbf{r}_{ref}$.

Direction	Azim. θ [°]	Elev. ϕ [°]	Radius [m]
back	−90	0	1
	−45	0	1
left	0	0	1
	45	0	1
front	90	0	1
	−90	40.6	1.01
	−45	40.6	1.01
	0	40.6	1.01
	45	40.6	1.01
	90	40.6	1.01

Smallest arrows show the used directions in the horizontal plane.

FIG. 2. (Color online) Used Cartesian and spherical coordinate systems (left) with the computed PRTF directions (right). The directions in the first column are for the left ear of a hypothetical head.

J. Acoust. Soc. Am. **146** (5), November 2019

Prepeliţă *et al.* 3635

3. Discretization error analysis in the frequency domain

Although not a new domain for error analysis,[56] a relevant and advantageous approach to the PRTF problem is to evaluate the convergence and the discretization error in the frequency domain: as formally defined, the PRTFs effectively become *steady-state* in the frequency domain after a minimal simulated time.

There are several advantages to studying the PRTF discretization error in the frequency domain. First of all, the PRTF problem becomes insensitive to the bandwidth of the initial conditions (see Sec. II D): the norm of the initial data will cancel out due to the pressure division in Eq. (1)—assuming a sampled excitation signal and a linear grid transfer function. Consequently, the used source would not require volumetric scaling of the amplitude for a monopole[29,57] or spatial distribution for a volumetric source (Ref. 19, p. 173). Moreover, this also eliminates a type of input error commonly referred to as *system excitation* (Ref. 20, p. 558) for a potential validation study. Similarly, the source/receiver interpolation-induced errors could cancel out during the frequency division. In addition, using only a subset of the Fourier coefficients effectively smooths the solution and initial conditions.

Employing the discrete Fourier transform (DFT) sampling of the DTFT spectrum, Eq. (6) can be written as

$$\widetilde{P}_{\mathfrak{r}_1}[\omega, \Delta T, \Delta X] = P_{\mathfrak{r}_1}[\omega] + \mathcal{E}_t[\omega]\Delta T^2 + \mathcal{E}_x[\omega]\Delta X^q + \text{HOT}[\omega]. \tag{12}$$

The simulated PRTF can be expressed in the frequency domain using Eqs. (1), (12), and a geometric series expansion[58] as

$$\begin{aligned}\widetilde{\text{PRTF}}_{\mathfrak{r}_1}[\omega, \Delta T, \Delta X] = &\text{PRTF}_{\mathfrak{r}_1}[\omega] + C_{T,\mathfrak{r}_1}[\omega]\Delta T^2 \\ &+ C_{X,\mathfrak{r}_1}[\omega]\Delta X^q + C'_{X,\mathfrak{r}_1}[\omega]\Delta X^2 \\ &+ \text{HOT}[\omega],\end{aligned} \tag{13}$$

where $\text{HOT} = O(\Delta X^{q+2})$ while $C_T[\omega]$ and $C_X[\omega](+C'_X[\omega])$ are the new temporal and spatial principal error terms, respectively.

Here, "h-extrapolation"[35] is used which involves the quantification of the discretization error employing successive grid refinements using a *grid refinement ratio* $\mathfrak{r}$ defined (Ref. 19, p. 109) for structured grids as

$$\mathfrak{r}_{ij} = \frac{\Delta X_j}{\Delta X_i} = \frac{f_{si}}{f_{sj}}, \tag{14}$$

where f_{si} is the sampling frequency for grid i. A minimum of $\mathfrak{r} \geq 1.1$ is recommended in practice (Ref. 19, p. 124) for a simple grid topology (Ref. 20, p. 311).

In the absence of round-off divergence, the error of lowest order will dominate as $\Delta X \to 0$, yielding an observed order of accuracy q_{obs} in Eq. (13) with a corresponding principal error term C^{PRTF},

$$\begin{aligned}\widetilde{\text{PRTF}}_{\mathfrak{r}_1}[\omega, \Delta T, \Delta X] = &\text{PRTF}_{\mathfrak{r}_1}[\omega] \\ &+ C^{\text{PRTF}}_{\mathfrak{r}_1}[\omega]\Delta X^{q_{\text{obs}}} + \text{HOT}[\omega],\end{aligned} \tag{15}$$

where the Courant grid ratio $\lambda_\mathcal{C}$ is used to exchange ΔT to ΔX.

Evaluating the observed convergence rate q_{obs} can be a good indicator to whether asymptotic range is attained: asymptotic range can be considered if $q_{\text{obs}} = \min(g, q)$, with a typical tolerance[59] of, e.g., $\pm 10\%$ (Ref. 20, p. 326).

Based on the point Fourier coefficients, the observed order of accuracy can be determined as

$$q_{\text{obs}}[\mathfrak{r}, \omega] = \frac{\log\left(\frac{|\widetilde{\text{PRTF}}_3[\omega] - \widetilde{\text{PRTF}}_2[\omega]|}{|\widetilde{\text{PRTF}}_2[\omega] - \widetilde{\text{PRTF}}_1[\omega]|}\right)}{\log(\mathfrak{r})}, \tag{16}$$

where $\widetilde{\text{PRTF}}_i[\omega]$ represents the simulated PRTF on grid ΔX_i with $\Delta X_1 < \Delta X_2 < \Delta X_3$ and consistent grid refinements $\mathfrak{r} = \mathfrak{r}_{12} = \mathfrak{r}_{23}$.

To study the convergence based on the PRTF magnitude, a power series expansion of $f(x) = \sqrt{1+x}$ can be used together with Eq. (15),

$$\begin{aligned}|\widetilde{\text{PRTF}}_{\mathfrak{r}_1}[\omega, \Delta T, \Delta X]| = &|\text{PRTF}_{\mathfrak{r}_1}[\omega]| \\ &+ C^{|\text{PRTF}|}_{\mathfrak{r}_1}[\omega]\Delta X^{q_{\text{obs}}} + \text{HOT}[\omega].\end{aligned} \tag{17}$$

Ignoring the HOT in Eq. (17) yields

$$q_{\text{obs}}[\mathfrak{r}, \omega] = \frac{\log\left(\frac{|\widetilde{\text{PRTF}}_3[\omega]| - |\widetilde{\text{PRTF}}_2[\omega]|}{|\widetilde{\text{PRTF}}_2[\omega]| - |\widetilde{\text{PRTF}}_1[\omega]|}\right)}{\log(\mathfrak{r})}. \tag{18}$$

Equation (17) is also valid on the decibel scale—since results were similar, they are omitted in the present work. Equation (18) has the advantage over Eq. (16) in that it is insensible to grid-dependent phase errors for fixed ω.

In practice, the derivation in Eqs. (12)–(16) tacitly assumes that the calculated discrete Fourier coefficients converge to the continuous ones at least as fast as q_{obs}. This is true, within machine epsilon,[60] for the usual midpoint/trapezoidal calculation of the DFT coefficients on equispaced temporal grids and band limited continuous functions sampled below Nyquist (see, e.g., Corollaries 2.3 and 5.3 in the work by Trefethen and Weideman[61]).

To estimate the discretization error, a minimal of two separate grids i and j are usually used to compute an asymptotic error estimate E_{ij} of order $O(\Delta X^{q+1})$ (see, e.g., Chap. 5 in the work by Roache[19]). Since E_{ij} is approximate, a safety[19,62] factor acting as a "coverage factor" $C_f \geq 1.0$ is usually introduced to conservatively scale E_{ij}, e.g., the grid convergence index (GCI) (Ref. 19, pp. 112–114). The C_f notation is chosen to avoid confusion with the sampling frequency f_s.

For example, an uncertainty band for the error of interest $E_{\text{dB}}[\omega] = 20\log_{10}|\widetilde{\text{PRTF}}_i[\omega]| - 20\log_{10}|\text{PRTF}[\omega]|$ can be obtained using the power rule (Ref. 63, p. 18) in relative error estimation together with the monotonicity of the logarithm function to include the commonly-used GCI,

$$|U_{\text{dB}}[\omega]| \leq \log_{10}\left(1 + 20 C_f \left|\frac{|\widetilde{\text{PRTF}}_2[\omega]| - |\widetilde{\text{PRTF}}_1[\omega]|}{|\widetilde{\text{PRTF}}_1[\omega]|(\mathfrak{r}^q - 1)}\right|\right), \tag{19}$$

where q is usually based on the observed convergence of the magnitude in Eq. (18) if some acceptable[59] asymptotic range is observed.

4. Regression models in convergence

In complex practical applications, the estimated q_{obs} values could lose precision and show the so-called scatter in the data.[64] Potential causes of scatter in q_{obs} include: error cancellation,[20] the round-off error on finer grids,[64] the grid[20,64] and boundary[18] modelling errors, and the actual function of the continuous solutions.[65,66] To account for such behavior, Eça and Hoekstra[64] introduced a least squares analysis of convergence. If the regression model is used for prediction, it is important to pick the correct model. From a regression perspective, both *a priori* (e.g., knowledge of error behavior) and *a posteriori* (e.g., hypothesis testing on model parameters) information can be used to correctly choose the regression model.

Based on the error analysis in Sec. II D, the lowest convergence rate is first-order due to the voxelization process. However, if any PRTF feature is linked to volumes of the pinna cavities, the third-order volumetric convergence of the voxelization process will be seen as second-order due to the update scheme. Finally, first-order convergence can also be observed if any non-rigid BC in the computation domain is close enough to the receivers (such that, e.g., the first-order error propagates to the receiver without strong $1/|\mathbf{r}|$ decay from the propagation on the continuous solutions). Similar to Eça and Hoekstra,[64] the following linear regression models based on magnitude are considered:

- first-order asymptotic model,

$$|\widetilde{\text{PRTF}}_{\mathbf{r}_1}[\omega, \Delta X]| = |\text{PRTF}_{\mathbf{r}_1}[\omega]| + C_1[\mathbf{r}_1, \omega]\Delta X, \quad (20a)$$

- second-order convergence,

$$|\widetilde{\text{PRTF}}_{\mathbf{r}_1}[\omega, \Delta X]| = |\text{PRTF}_{\mathbf{r}_1}[\omega]| + C_2[\mathbf{r}_1, \omega]\Delta X^2, \quad (20b)$$

- combined first- and second-order type,

$$|\widetilde{\text{PRTF}}_{\mathbf{r}_1}[\omega, \Delta X]| = |\text{PRTF}_{\mathbf{r}_1}[\omega]| + C'_{12}[\mathbf{r}_1, \omega]\Delta X + C''_{12}[\mathbf{r}_1, \omega]\Delta X^2, \quad (20c)$$

where $|\text{PRTF}_{\mathbf{r}_1}[\omega]|$ represents the sought asymptotic magnitude at location $\mathbf{r}_1$. In addition, Eça and Hoekstra[64] also proposed the following non-linear regression model:

$$|\widetilde{\text{PRTF}}_{\mathbf{r}_1}[\omega, \Delta X]| = |\text{PRTF}_{\mathbf{r}_1}[\omega]| + C_q[\mathbf{r}_1, \omega]\Delta X^q, \quad (21)$$

which can also be used to quantify q_{obs} from the least-squares fit of the parameter q. There are different ways to estimate q in Eq. (21), e.g., using non-linear regression, solving non-linear equations,[64] or through the Box-Tidwell[67] procedure.

The above models assume that ΔX is not too small such that round-off divergence is observed in which case error/asymptotic estimation becomes more difficult.

By utilizing the regression models proposed by Eça and Hoekstra,[64] the asymptotic solution $\text{PRTF}_{\mathbf{r}_1}[\omega]$ becomes a random variable as a parameter of a probabilistic model. As such, one can quantify the uncertainty of the asymptotic solution through the derivation of confidence intervals (CIs) as long as the probabilistic models are used appropriately. The asymptotic solution can be predicted from the regression models based on the mean output of each model as

$$|\text{PRTF}_{\mathbf{r}_1}[\omega]| \approx \mathbb{E}\left[|\widetilde{\text{PRTF}}_{\mathbf{r}_1}[\omega, \Delta X]| \,|\, \Delta X = 0\right], \quad (22)$$

where $\mathbb{E}$ is the expected value operator. In practice, $|\text{PRTF}_{\mathbf{r}_1}[\omega]|$ in Eq. (22) is considered the intercept yielded by the least-squares fit of the regression models.

Parametric methods—The CIs can be estimated based on the usual covariance of the inputs and variance of the residuals [see, e.g., Sec. 3.4 from the work by Montgomery *et al.* (Ref. 68, p. 95)]. Such CIs are reliable when the regression model assumptions are satisfied (Ref. 68, p. 122 and Ref. 69, p. 28): (i) ΔX is measured without error, (ii) the residuals of the regression model are independent of each other, and (iii) the residuals are normally distributed with (iv) constant variance. For example, gross violations of normality could have a serious effect on the estimated CIs (Ref. 68, p. 139). Although (i) is satisfied due to the uniform and structured grid used, it is difficult to give strong arguments for (ii)–(iv) given the problem at hand. The usual visual techniques to assess normality are difficult to apply to the PRTF problem due to the large amount of data. One alternative is to use statistical tests of normality, which might not be very reliable for a small number of grids N_g.

For each frequency, homoscedasticity (iv) is likely violated.[18] As such, the weights introduced by Eça and Hoekstra[64]

$$W_i = \frac{\dfrac{1}{\Delta X_i}}{\displaystyle\sum_{j=1}^{N_g} \dfrac{1}{\Delta X_j}}, \quad (23)$$

for weighted least squares models could be helpful.

Non-parametric methods—The alternative to the Gaussian-based CIs is to use non-parametric estimation methods. One such technique is bootstrapping[70] which, in its basic form, only relies on the residual independence (ii) assumption. Such assumption may still be difficult to motivate for minute changes in ΔX. In the context of regression, two main bootstrapping methods exist (Ref. 68, p. 494): bootstrapping pairs and bootstrapping residuals. Bootstrapping pairs is generally used whenever there is increased doubt about the assumed regression model. There are also different methods to estimate the CI: the *bias-corrected and accelerated* (BC_a) method is chosen which corrects for bias and skewness in the bootstrap samples and is "second-order" accurate [i.e., estimate error is proportional with $O(1/N_g)$]—see Chap. 14 from Efron and Tibshirani.[70]

Such uncertainty estimates are different than the estimates proposed by Eça and Hoekstra[64] based on the safety

J. Acoust. Soc. Am. **146** (5), November 2019

Prepeliţă *et al.*   3637

factor C_f. Nevertheless, if required, C_f can be included in the analysis as an appropriate coverage factor.

5. PRTF simulations

A total of 10 directions are simulated (see Fig. 2) on $N_g = 6$ grids and a constant grid refinement ratio of

$$\mathfrak{r}_{i,i+1} = 1.1 := \widetilde{\mathfrak{r}}, \tag{24}$$

with $i \in \{1, 2, \ldots, N_g - 1\}$. To directly apply Eqs. (16)–(19), the same discrete frequencies $f_k = \omega_k (2\pi)^{-1}$ must be sampled with the DFT on each grid. This implies a consistent frequency resolution $\Delta f = 1/t_{\text{obs}}$, where t_{obs} is the observation interval

$$t_{\text{obs}} = N_i \Delta T_i = t_{\text{sim}i} + \Delta T_i, \tag{25}$$

where $N_i \in \mathbb{N}^*$. To obtain consistency of t_{obs}, the sampling frequency f_{si} on grid i was adjusted incrementally from an initial value that satisfied the grid refinement ratio $\mathfrak{r}_{i,i+1} = 1.1$ in Eq. (14) until Eq. (25) was satisfied for $t_{\text{obs}} = 6.25$ [ms]. Since t_{obs} and $\lambda_{\mathcal{C}}$ were fixed while ΔX changed given an integer sampling frequency $f_{si} \in \mathbb{N}^*$ enforced by the solver, it is not always possible to perfectly preserve both $\mathfrak{r}_{ij}$ and Δf.

The chosen frequency resolution is $\Delta f = 160$ [Hz]. A sub-millimeter voxel is desirable for increased precision of the calculated FDTD PRTFs at higher frequencies.[18] The smallest voxel is limited by the available resources. The voxel sizes used vary from 0.95 to 0.59 [mm]—Table III shows the details of the convergence study.

The surface boundary impedance for the pinna, ear-canal blocking, and surface of the microphone was set as fully rigid $\beta = 0$. For all simulations, a temperature of 294.78 [K] was used which entailed a dry-air sound speed (Ref. 71, p. 121) of about 344.34 [m/s].

6. PRTF results and discussion

To avoid ripple distortions in the PRTF spectra due to "edge effects" between DFT periods, a continuous Gaussian

window was sampled at $t_n = n \Delta T_i$ ($n \in \mathbb{N}$) and applied to both the interpolated simulated temporal signals in Eq. (1),

$$w(t) = e^{-\alpha^2 (t - t')^2}, \tag{26}$$

where $t' = t_{\text{obs}}/2$ and the parameter α was chosen such that the amplitude of the window had negligible values at the beginning and end of the observation interval: $w(t_{\text{obs}}) \approx 1 \times 10^{-7}$.

Due to the frequency division in Eq. (1), the ΔT scaling in the DFT cancels out and the PRTFs were computed with the usual fast Fourier transform (FFT) routines which are working on normalized temporal grids (Ref. 72, p. 3). A discrete delta sequence was used as the input to the driving soft source for both simulations in Eq. (1). No circular shifts were applied to the computed $\widetilde{\text{PRTF}}$.

In the following, unless otherwise mentioned, the results are presented for the interpolated PRTFs (both source and receiver—see Sec. III B 1): interpolation was done on the center of the source voxel from grid 5. The analysis is limited to 24 [kHz] yielding a total of $N_{\text{freqs}} = 151$ positive frequency bins.

Assessing asymptotic range. Since an *a posteriori* error estimation in Eq. (19) may be problematic if the asymptotic range is not attained,[35] a first analysis of the computation of the observed convergence rate q_{obs} is performed. Q_{obs} can be computed either based on three grids [Eqs. (16) and (18)] or estimated based on the non-linear regression model in Eq. (21). Results for one typical direction are presented in Figs. 3 and 4. Results show similar behavior for the other directions. Undefined results in $\mathbb{R}$ such as the logarithm of a negative number are excluded from the plots.

The three-grid estimation of q_{obs} is shown in Fig. 3. In this case, since 6 grids are available for each frequency bin, q_{obs} can be estimated 4 times based on three consecutive grids (i.e., $\{j, j+1, j+2\}, j = 1 \ldots 4$ grid triplets) using $\mathfrak{r} = \widetilde{\mathfrak{r}}$ and twice on every other grid (i.e., $\{1, 3, 5\}, \{2, 4, 6\}$ grid triplets) using $\mathfrak{r} = \widetilde{\mathfrak{r}}^2$ in Eqs. (16) and (18). In the calculation of q_{obs} in Eqs. (16) and (18), the ideal value of $\widetilde{\mathfrak{r}} = 1.1$ was used and not the empirical values in Table III—results

TABLE III. Grids used in the PRTF convergence study. Interpolation done on source/receiver location from grid 5. The voxel sizes ΔX and N_{voxels} are rounded to two decimal places for their units. N_{voxels} represents the total number of voxels used in simulations excluding the halos on each MPI node. N_{Nodes} represents the number of MPI nodes—see Appendix B. $\mathfrak{r}_{i,i+1}$ also contains the deviation from the chosen $\widetilde{\mathfrak{r}}$ in Eq. (24). N_{DFT} represents the number of temporal samples used to compute the DFT (i.e., the simulation interval in samples) such that a Δf frequency resolution is attained in the DFT. N_{freqs} represents the number of positive frequencies used in the analysis, while N_{dirs} represents the total number of PRTF directions.

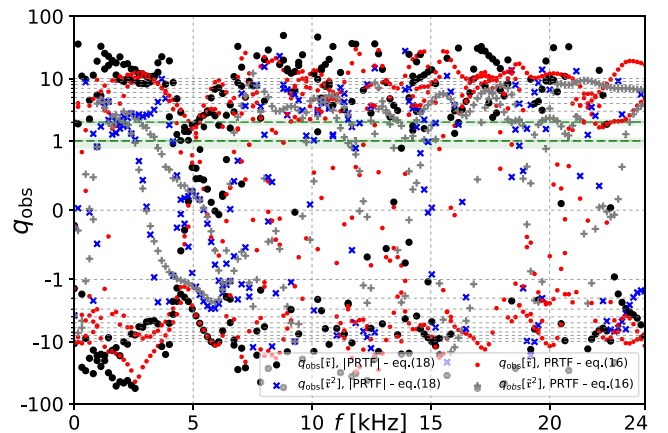| Grid	f_s [Hz]	ΔX [mm]	$\mathfrak{r}_{i,i+1}$ $[\widetilde{\mathfrak{r}} + \epsilon]$	N_{Nodes}	N_{voxels} [$\times 10^9$]	N_{DFT} [samples]
1	1 014 240	0.59	—	7	100.47	6339
2	922 080	0.65	$1.1 + 5.2 \times 10^{-5}$	5	75.33	5763
3	838 240	0.71	$1.1 + 1.9 \times 10^{-5}$	4	56.72	5239
4	762 080	0.78	$1.1 + 6.3 \times 10^{-5}$	3	42.62	4763
5	692 800	0.86	1.1	3	31.98	4330
6	629 760	0.95	$1.1 + 1.0 \times 10^{-4}$	3	23.98	3936
	$\Delta f = 160$ [Hz]		$N_{\text{freqs}} = 151$			$N_{\text{dirs}} = 10$

FIG. 3. (Color online) Estimated observed order of accuracy q_{obs} for direction $(-90°, 0°)$ based on magnitude [Eq. (18)] and on complex-values [Eq. (16)]. $q_{\text{obs}}[\widetilde{\mathfrak{r}}]$ uses three consecutive grids while $q_{\text{obs}}[\widetilde{\mathfrak{r}}^2]$ uses three alternate grids. Horizontal dashed lines show expected first- and second-order q_{obs} embedded in ± 10[%] intervals.
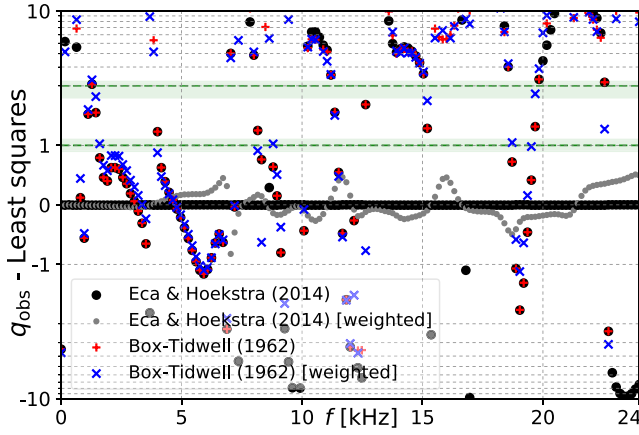
FIG. 4. (Color online) Observed order of accuracy q_{obs} based on Eq. (21) and different calculation methods for direction $(-90°, 0°)$. y-axis is truncated to $[-10, 10]$. Green dashed lines show expected first- and second-order q_{obs} embedded in $\pm 10[\%]$ intervals.
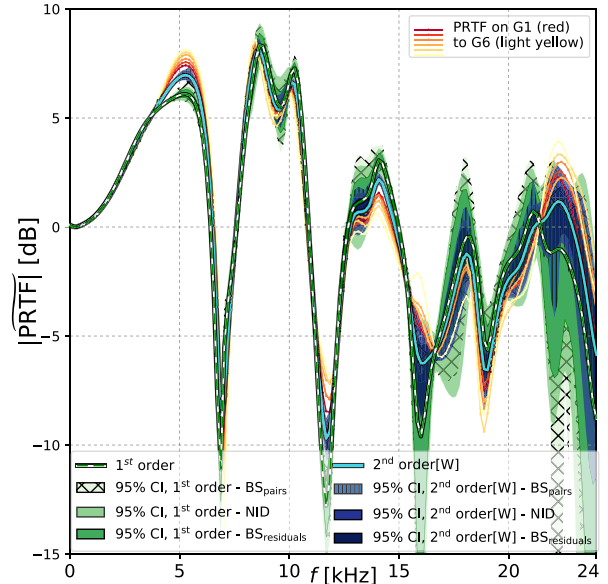

FIG. 5. (Color online) Single-grid PRTFs (red) and three CI estimate types for the interpolated asymptotic solutions: based on the normality assumption (NID) and based on bootstrapping (BC$_a$—pairs, BC$_a$—residuals). Results shown for a first-order [Eq. (20a)] and a weighted second-order [Eqs. (20b) and (23)] models.

were almost identical when q_{obs} was numerically determined[35] for $\mathfrak{r}_{12} \neq \mathfrak{r}_{23}$. Results show a high amount of scatter with unreasonable values of q_{obs}, for instance, the divergence is worse than $O(\Delta X^{-10})$ for some frequency bins. Data for PRTFs directions close to the dispersion-free grid diagonal [i.e., $(-45°, 40.6°)$ and $(45°, 40.6°)$] did not exhibit improved results. Moreover, the discrimination ratio[64] does not show any consistent bandwidth of monotonic convergence.

It is unclear why such unreliable results are obtained for the three-grid estimates of q_{obs}. Lower frequencies might not show convergence due to the round-off noise floor: for instance, the $160\,Hz$ frequency bin is sampled more than 2000 times in a wavelength. The grid size ΔX might still be too large for higher frequencies where solution could be affected by pollution error even at the current voxel sizes employed, poor precision in the PRTF data due to the voxelization process, and small refinement ratios $\mathfrak{r}$.

Too small $\mathfrak{r}$ are expected to cause too little changes in the computed solution (Ref. 20, p. 331) and would render the obtained data unreliable for a convergence study. Figure 3 shows that computing q_{obs} with the larger grid refinement ratio of $\widetilde{\mathfrak{r}}^2 = 1.21$ only provides marginal improvements: the range of values for q_{obs} diminishes but not to a useful extent. Thus, a much larger refinement ratio $\mathfrak{r}$ might be needed which conflicts with the limitations in the methods: memory limitations for lower ΔX and increased solution scattering[18] for larger ΔX. Finally, a clear convergence trend is seen in the PRTF magnitudes as ΔX is decreased: see the convergence of the "concha depth"[73] mode around 5 [kHz] in Fig. 5.

Thus, estimating q_{obs} does not seem to be well-conditioned for the current problem and models: the random error in the voxelization process coupled with numerical sensitivity might render the three-grid method unreliable. Since solutions depend on the boundary, such voxelization-induced "boundary noise" could translate into slight changes in the asymptotic solutions. The expected strong sensitivity of the PRTFs to the pinna shape further aggravates such changes. Thus, it is possible that computed solutions from different grids belong to neighboring analytic solutions[47]

and render the estimation of q_{obs} unusable at a single point in space. Spatially averaged solutions might be less sensitive to such small boundary changes.

Consider now the estimation of q_{obs} based on the non-linear regression model. Figure 4 shows the estimated q_{obs} based on Eq. (21). Results are shown for both weighted [see Eq. (23)] and non-weighted regression models. Compared to Fig. 3, results show less erratic results but are still unreliable: many frequencies far away from the direct current (DC) one (i.e., $\omega = 0$) show divergence with other frequencies showing unreasonably high convergence rates. For many frequency bins, results are similar for different methods of calculation for the non-weighted models. Similar to the last example in the work by Eça and Hoekstra, one reason for such results could be the small number of grids.[64] Non-linear regression was also applied to Eq. (21) but results were too sensitive to the starting values which were poorly estimated based on the three-grid calculations—see Fig. 3.

Based on the results in Figs. 3 and 4, it would be difficult to estimate a bandwidth where asymptotic range is attained. Thus, the commonly used two-grid error estimates such as Eq. (19) will yield unreliable results and cannot be used on the current simulated data with a high degree of confidence.

Estimating the asymptotic solution. Results of the predicted asymptotic solution by the linear regression models are shown in Figs. 5 and 6 for the $(-90°, 0°)$ direction. Results are similar for the other directions.

CI estimation—Notice first that although the plots in Figs. 5 and 6 are on the decibel scale, the uncertainty in the CI is *not* propagated through the logarithm function [see, e.g., Baird (Ref. 63, p. 19)]. Figure 5 shows the behavior of the three types of estimates for the CIs for two regression models: first-order and weighted second-order. A number of
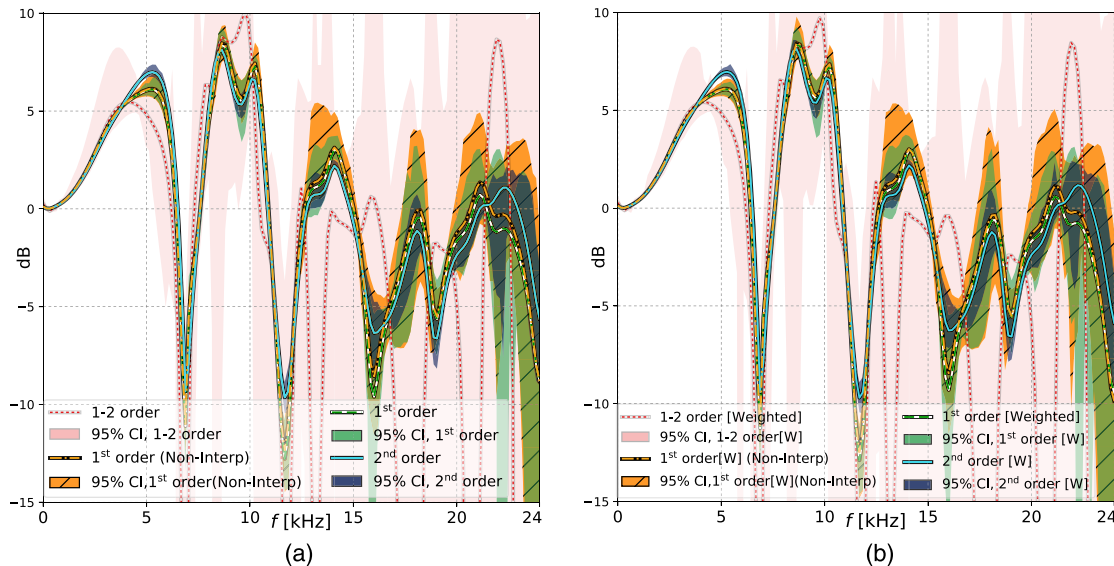
J. Acoust. Soc. Am. **146** (5), November 2019

Prepeliţă *et al.* 3639

FIG. 6. (Color online) Asymptotic solution and estimated CIs based on the models in Eqs. (20a)–(20c) unweighted (left) and weighted (right) for $(-90°, 0°)$ direction. The result for a first-order weighted model [Eq. (20a)] on the non-interpolated data are also shown. (a) Non-weighted and (b) weighted.

$B = 5000$ bootstrap replicates are used for the non-parametric estimates.[74] Results show that the two-tailed parametric CI estimates are usually within the nonparametric ones. Moreover, the tightest estimates are found by employing BC_a on bootstrapping residuals while the largest estimates are expressed through the BC_a estimates on bootstrapping pairs. Such results on the CIs generally extrapolate to all the considered linear regression models: no strong qualitative deviations were observed. Since no normality of residuals is required for the non-parametric CIs, they are to be preferred to the parametric CIs. If more conservative estimates of region of the asymptotic solution are preferred, CIs are better estimated with bootstrapping pairs.

Asymptotic predictions—The asymptotic predictions of the linear regression models in Eqs. (20a)–(20c) are shown in Fig. 6(a) together with the most conservative CI estimates. A first result is that the first- and second-order model in Eq. (20c) shows very poor results: predictions contain PRTF features which are not present in any computed solution—see Fig. 5. Moreover, the model predicts unphysical discontinuities or negative magnitudes. Unreasonably large CIs also suggest a poor fit. Finally, *a posteriori* significance tests for the two regressors ΔX and ΔX^2 from model (20c) showed significance in less than 2% of cases for both weighted and non-weighted models. The significance was tested such that, e.g., $H_0 : C_{12}'' = 0$ was rejected (Ref. 68, p. 84) for a p-value ≤ 0.005 with the data pooled over all frequency bins and directions. Such results are considered poor enough to show the ill-fit of such regression model. Consequently, the first- and second-order model in Eq. (20c) is excluded from further analysis.

However, it is not so straightforward to exclude one of the remaining two linear regression models: both models predict similar asymptotic solutions which are consistent with the computed solutions on the six utilized grids. One way to assess the fit of the regression models is to explore the coefficient of determination R^2. For all the $N_{freqs} \times N_{dirs} = 1510$ data points, R^2 for the first-order model in

Eq. (20a) is larger than for the second-order model in Eq. (20b) in 49.21% cases. For the weighted linear models, 50.73% of the data points indicate a better fit for the first-order model based on R^2. Thus, neither of the two models can be excluded based on aggregated results. A frequency-dependent analysis of R^2 shows that the first-order model generally fits the data better up to about 8.5 [kHz] and other sporadic frequency bands such as $[11.5 - 12.5]$ [kHz] and $[19 - 20]$ [kHz]. Such results are seen for both weighted and non-weighted linear models—results not shown.

In regression analysis, model selection strategies based on "domain knowledge" (Ref. 68, pp. 285–286) are favored to descriptive data-driven selection. The non-interpolated PRTFs can be used as a model selection criterion: the PRTFs will converge in a first- order fashion due to source/receiver inconsistencies (see Sec. II D) assuming other errors such as the pollution error are not dominating. The source/receiver location for the non-interpolated PRTFs are calculated in a nearest-neighbor fashion, at a voxel close to the continuous location given by grid 5.

Figures 6(a) and 6(b) both contain the first-order prediction of the asymptotic solution for the non-interpolated PRTFs together with the pair-bootstrapped CIs. The first-order regression model in Eq. (20a) was used for the non-interpolated PRTFs. It can be seen that for the concha depth mode, the second-order model predicts an inconsistent solution: the CIs are disjoint. This result is consistent with the frequency-dependent analysis of the coefficient of determination R^2. Results suggest that, at low frequencies, the simulations are dominated by first-order errors originating in the voxelization process.

For the other PRTF directions in the study, in addition to the general misprediction of the second-order model of the asymptotic amplitude of the concha depth mode, its CIs do not overlap with the non-interpolated ones at various 1–2 kHz wide frequency bands (results not shown). Moreover, although not statistically significant, the predicted

asymptotic solution from Eq. (22) is more consistent with the first-order model than the second-order one: one could see small deviations in the peaks and notches of the PRTF spectra relative to the non-interpolated PRTF.

It should be mentioned that: (i) for direction $(45°, 0°)$ the CIs overlap for the three regression models: first-order, second-order, and non-interpolated first-order; (ii) compared to the second-order regression model, the first-order model fails to predict one PRTF notch for direction $(90°, 40.6°)$: the asymptotic value of the magnitude is negative.

Figure 6(b) shows the weighted results. Results are highly similar with the non-weighted ones in Fig. 6(a). Both the asymptotic solutions and the CIs in the weighted case undergo small corrections: the asymptotic solutions change mostly less than 0.5 [dB] for the first- and second-order models while the CIs are generally smaller for the weighted models. The 0.5 [dB] value is estimated based on a histogram of the difference for the data pooled across all frequencies and directions—histogram not shown. All the previous results from non-interpolated regression models are found adequate also for the weighted regression models. Since the precision of computed PRTFs increases with smaller voxel,[18] the weighted models are preferred over non-weighted models and the small corrections are considered improvements in the accuracy of predictions.

Interpolation impact—The effect of interpolation is also seen: using interpolated PRTFs improves the precision of the estimated asymptotic solutions. Although not shown, the largest effect on the precision is for interpolation within the concha volume (here, source interpolation) as compared to interpolation in the far-field. Moreover, using the weights in Eq. (23) appears to partly correct the prediction bias in the asymptotic solution in Eq. (22) of the non-interpolated PRTFs relative to the interpolated PRTFs. Consequently, since the boundary $\partial\mathcal{D}$ gives the lowest order of convergence for the employed discrete models, a weighted least-squares could be used without the need to interpolate the solution if lower precision is acceptable.

Peak/Notch estimation—Of interest for the PRTF problem are the frequency locations of the peaks and notches and their convergence. Such PRTF features were coarsely extracted in a nearest-neighbor fashion and shown in Fig. 7 for the same $(-90°, 0°)$ direction. Here, only the first-order model is considered. Despite the $O(\Delta f)$ error in frequency estimation, it can be seen that such features undergo corrections of various degrees. The amount of correction was also found to be direction-dependent. Moreover, the individual computations could display spurious features compared to the asymptotic solution, mostly below 20 [kHz]. Similarly, the asymptotic solution could show extra features above 20 [kHz]—nevertheless, such conclusion is weak since the uncertainty is high at such frequencies. It is difficult to say based on the present results whether any PRTF feature converges non-linearly in ΔX which might indicate a volumetric dependence.

IV. DISCUSSION

Results in Figs. 3 and 4 show the difficulty in estimating the computational errors in practical problems with complex geometries: asymptotic range does not seem to be attained even on the submillimeter grids used. Depending on frequency, various sources of error and their interaction could be responsible for such behavior—see Secs. III B 6 and II D. Given the present models, one solution would be to increase the computational accuracy: using double precision for lower frequencies and smaller ΔX such that asymptotic range is reached within some bandwidth. However, such solution is presently unreachable due to restrictions in computing memory: the simulation on grid 1 already uses more than 100×10^9 voxels.

Alternatively, regression models will not only predict the asymptotic solution, but will also reflect the quality of such predictions: larger CIs of the asymptotic solution will signal stronger departures from the expected asymptotic regime—equivalently, a reliability decrease of the computed solution. However, to avoid both prediction bias and incorrect CIs, the asymptotic behavior of the errors present in the computations needs to be understood such that the correct regression model is applied.

Since the mathematical theory predicts that the discretization error is a bias in the solution, statistical estimates for computed solutions are sometimes discredited.[23,75] Nevertheless, the discontinuity in the convergence of the boundary $\partial\mathcal{D}$ (which may cause, e.g., jumps in the error asymptotes[47] as $\Delta X \to 0$) motivates the random treatment of the convergence. Moreover, the commonly used techniques in error estimation were shown to be difficult to apply for the present problem and associated parameters. The estimated asymptotic solutions also show that a two-grid error estimate such as the GCI would have been unreasonably large for the PRTF/HRTF problem. Additionally, the asymptotic solution was estimated based on the asymptotic behavior of the discretization error of lowest order which should persist, as $\Delta X \to 0$, until round-off error will cause divergence from the true solution. This also motivates predictions using least squares outside the observed grid interval: round-off divergence would dominate the results as ΔX approaches 0. Finally, no noticeable divergence is qualitatively observed at low frequencies.

Nevertheless, such regression models are not perfect. Potential caveats in faulty model assumptions were mentioned in Sec. III B 4: unless the independence assumption in the residuals is strongly violated (see, e.g., Sec. II D), the given estimates and CIs are expected to have a reasonable degree of reliability.
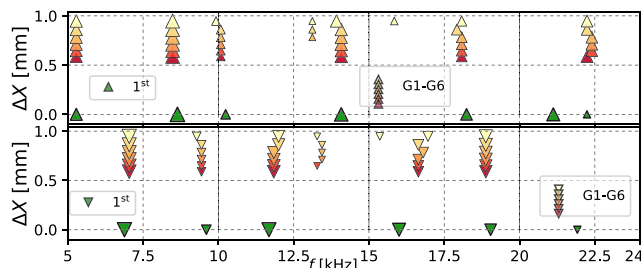

FIG. 7. (Color online) Peaks (top) and notches (bottom) on each grid in Table III and the asymptotic solution for the first-order model in Eq. (20a). Marker size is proportional to the log of the prominence in dB.

J. Acoust. Soc. Am. **146** (5), November 2019

Prepeliţă *et al.* 3641

Although the fit at higher frequencies is not much better than a second-order model, the first-order regression model is still considered representative for the used discrete models since: (i) it better matches the non-interpolated predictions, (ii) there is no previous data supporting volumetric ear modes (most previous studies only consider distances[17,76]), and (iii) it accounts for the smallest sources of error (see Sec. II D). Besides, larger CIs could signal a poor fit.

An alternative would be to use different regression models depending on frequency but this could cause discontinuous asymptotic solutions. Since pollution error could be of concern at higher frequencies and in the spirit of more conservative estimates, the CIs calculated with the non-parametric bootstrapping BC_a-pairs are advised.

The present paper only deals with the quality of finite-difference PRTF calculations and not with their validity in predicting real-world PRTFs. Such model legitimacy needs to be assessed in a separate validation study where FDTD predictions along with their estimated computational errors are compared with real-world measurements.

V. CONCLUSION

Individual computations are not necessarily a faithful representation of wave-based formal solutions when complex geometries are involved: they could embed errors which should not be assumed negligible. The present work showed that the current state in HRTF/PRTF simulation literature which involve a single computation could yield erroneous results: for each input parameter such as β, single-grid computed solutions could be biased relative to the formal solution. Reliability assessment of the computational result should always be performed.

The employed FDTD solver was verified using relevant methods from the V&V literature—a mandatory step prior to the investigation of the error in the simulated HRTFs/PRTFs.

The error in computed PRTFs for the ipsilateral ear was assessed for a blocked-meatus location through a convergence study on sub-millimeter grids. Since no clear asymptotic range was observed, the commonly employed techniques based on Richardson extrapolation were found inapplicable for the used grids and models. Estimates of the asymptotic solution using weighted[64] regression models fitted on multiple grids were found more adequate. The method also provides CIs for the asymptotic solutions which could provide reliability information for any validation study. The non-parametric bias-corrected and accelerated CI estimation method based on bootstrapping pairs provided more conservative estimates with better justified assumptions.

The estimated asymptotic solution was found less reliable at high frequencies and at notches in the PRTF features even for the unprecedented grid spacing used. Moreover, the proposed method requires a thorough understanding of the sources of error in order to employ the correct regression model: prediction bias is otherwise expected. In the present case, a first-order regression model was found adequate. It was also found that, due to the stair-stepped boundaries, source and receiver interpolation does not appear to be mandatory. However, interpolation improves the precision of the estimated asymptotic solution.

Evaluation of the magnitude of the computational errors or asymptotic estimation of the solution such as given in the present work are a prerequisite for a correct assessment of modeling errors and assumptions in wave-based HRTF simulations. Due to complex interactions among numerical errors even for a simple wave model such as the SRL scheme, using HRTF/PRTF simulations as a reliable black-box prediction tool seems presently unfounded: no single-grid computation is necessarily correct in the entire audible range even when employing submillimeter voxels; error assessment is recommended. The proposed procedure is one such evaluation method.

APPENDIX A: MATHEMATICAL SYMBOLS AND CONVENTIONS

In the present text, the lattice that the FDTD update operates upon and tessellates the space-time will be referred to as *grid* while the term *mesh* will denote any triangulated representation of a continuous surface. A uniform and structured 3D Cartesian grid is used, formed by cubic control volumes which are named *voxels* in the present work. The grid spacing will be denoted by ΔX, the time step by ΔT, and the "sampling" frequency as $f_s = 1/\Delta T$.

The term *model* is used throughout the work in a broad sense as a representation of some system/process or even another model without circular "referencing"—see also the AIAA definition (Ref. 20, p. 92).

Signals in the frequency domain are denoted by uppercase letters while lowercase letters are used for their time-domain representation. The FDTD and semi-discrete [e.g., $P_j(t)$ in Eq. (5)] dependent variables are written in uppercase and the superscript indexes time while the subscript indexes integer 3D lattice coordinates.

3642   J. Acoust. Soc. Am. **146** (5), November 2019

Prepeliţă *et al.*

Parentheses are used for arguments in the case of continuous signals, while square brackets are used for discrete signals. Ω is used for the angular frequency [rad/s] for continuous temporal signals, while ω is for the angular frequency of discrete-time signals. The set of natural numbers is denoted by $\mathbb{N}$ (with $\mathbb{N}^* := \mathbb{N} - \{0\}$), integer numbers by $\mathbb{Z}$ and $\mathbb{R}$ denotes the set of real numbers.

Contrary to the notation in the PDE literature, independent variables as subscripts to dependent variables are used as naming conventions: $p_t \neq \partial p / \partial t$ while $\partial_t p = \partial p / \partial t$.

APPENDIX B: SOFTWARE AND HARDWARE DETAILS

The FDTD implementation was developed on the GPU using CUDA kernels[77] and parallelized further using the MPI using a CUDA-aware MPI library.[78]

For the voxelization process, all triangle-voxel intersections are done in double precision. All FDTD simulations are done in single precision while the post-processing (such as the SciPy[79] v1.1.0 FFT algorithms) is implemented in Python 2.7.13 [Enthought Canopy (Version 2.1.9) Software, http://www.enthought.com] by using double precision NumPy[80] v1.15.4 arrays. For code verification, the analytical terms (i.e., initial conditions and forcing terms) are initially calculated in double precision.

For solution verification, the single term expansion with unknown q_{obs} from Eça and Hoekstra[64] is calculated naively by sweeping q_{obs} in $\Delta q_{obs} = 0.005$ steps and finding zero-crossing (including zeros) for the last non-linear equation in Appendix B.2 from the same work. The *Box-Tidwell* procedure is based on Fox's (Ref. 81, p. 312) R version (using a tolerance of 10^{-3} and a maximum of 1000 steps). For the weighted Box-Tidwell calculation, the ordinary least squares calls from the two fits used by the procedure are replaced by weighted least squares fits on the same data with the weights from Eq. (23). The linear regression prediction is based on the results from *statsmodel*[82] (Version 0.8.0) while the non-linear regression trials were done using the *scipy.optimize* package (using the Levenberg-Marquardt algorithm and explicitly defining the Jacobian). The *scipy.signal.find_peaks()* function is used to extract the features in Fig. 7 (feature height of 30 dB and width of Δf).

The BC_a bootstrapped CIs are computed by employing *scikits.bootstrap* (Version 1.0.0) python package (http://github.org/cgevans/scikits-bootstrap) which is based on the description given in Chap. 14 by Efron and Tibshirani.[70]

The final simulations were run on Amazon EC2 on *p2.16xlarge* instances running CentOS 7.3 in the same placement group. Each instance contained 16 NVIDIA K80 GPUs, totaling $16 \times 12 = 192$ GB GPU memory per node. The relevant software stack on the cluster consisted of *gcc* 4.8.5, *CUDA* toolkit 8.0, and *OpenMPI* 2.0.2. Synchronous MPI communication was used to avoid non-determinism concerns.[83]

[1] P. M. Hofman, J. G. A. Van Riswick, and A. J. Van Opstal, "Relearning sound localization with new ears," Nat. Neurosci. **1**(5), 417–421 (1998).

[2] E. M. Wenzel, M. Arruda, D. J. Kistler, and F. L. Wightman, "Localization using nonindividualized head-related transfer functions," J. Acoust. Soc. Am. **94**(1), 111–123 (1993).

[3] A. J. Hoogstrate, H. Van Den Heuvel, and E. Huyben, "Ear identification based on surveillance camera images," Sci. Justice **41**(3), 167–172 (2001).

[4] M. Morimoto and Y. Ando, "On the simulation of sound localization," J. Acoust. Soc. Jpn. (e) **1**(3), 167–174 (1980).

[5] F. L. Wightman and D. J. Kistler, "Headphone simulation of free-field listening. II: Psychophysical validation," J. Acoust. Soc. Am. **85**(2), 868–878 (1989).

[6] E. H. A. Langendijk and A. W. Bronkhorst, "Fidelity of three-dimensional-sound reproduction using a virtual auditory display," J. Acoust. Soc. Am. **107**(1), 528–537 (2000).

[7] R. L. Martin, K. I. McAnally, and M. A. Senova, "Free-field equivalent localization of virtual audio," J. Audio Eng. Soc. **49**(1/2), 14–22 (2001).

[8] P. Majdak, P. Balazs, and B. Laback, "Multiple exponential sweep method for fast measurement of head-related transfer functions," J. Audio Eng. Soc. **55**(7/8), 623–637 (2007).

[9] P. Dietrich, B. Masiero, and M. Vorländer, "On the optimization of the multiple exponential sweep method," J. Audio Eng. Soc. **61**(3), 113–124 (2013).

[10] G. Enzner, "3d-continuous-azimuth acquisition of head-related impulse responses using multi-channel adaptive filtering," in *2009 IEEE Workshop on Applications of Signal Processing to Audio and Acoustics*, New Paltz, NY (2009), pp. 325–328.

[11] B. F. G. Katz, "Boundary element method calculation of individual head-related transfer function. I. Rigid model calculation," J. Acoust. Soc. Am. **110**(5), 2440–2448 (2001).

[12] Y. Kahana and P. A. Nelson, "Numerical modelling of the spatial acoustic response of the human pinna," J. Sound Vib. **292**(1–2), 148–178 (2006).

[13] W. Kreuzer, P. Majdak, and Z. Chen, "Fast multipole boundary element method to calculate head-related transfer functions for a wide frequency range," J. Acoust. Soc. Am. **126**(3), 1280–1290 (2009).

[14] C. Jin, P. Guillon, N. Epain, R. Zolfaghari, A. van Schaik, A. Tew, C. Hetherington, and J. Thorpe, "Creating the Sydney York morphological and acoustic recordings of ears database," IEEE Trans. Multimed. **16**(1), 37–46 (2014).

[15] H. Ziegelwanger, P. Majdak, and W. Kreuzer, "Numerical calculation of listener-specific head-related transfer functions and sound localization: Microphone model and mesh discretization," J. Acoust. Soc. Am. **138**(1), 208–222 (2015).

[16] T. Xiao and Q. H. Liu, "Finite difference computation of head-related transfer function for human hearing," J. Acoust. Soc. Am. **113**(5), 2434–2441 (2003).

[17] P. Mokhtari, H. Takemoto, R. Nishimura, and H. Kato, "Frequency and amplitude estimation of the first peak of head-related transfer functions from individual pinna anthropometry," J. Acoust. Soc. Am. **137**(2), 690–701 (2015).

[18] S. Prepeliţă, M. Geronazzo, F. Avanzini, and L. Savioja, "Influence of voxelization on finite difference time domain simulations of head-related transfer functions," J. Acoust. Soc. Am. **139**(5), 2489–2504 (2016).

[19] P. J. Roache, *Verification and Validation in Computational Science and Engineering* (Hermosa Publishers, Albuquerque, NM, 1998).

[20] W. L. Oberkampf and C. J. Roy, *Verification and Validation in Scientific Computing*, 1st ed. (Cambridge University Press, New York, 2010).

[21] D. Lee and T.-S. Ahn, "A boundary element model for acoustic responses in the ear canal and its statistical validation and updating," J. Mech. Sci. Technol. **28**(4), 1203–1217 (2014).

[22] V. R. Algazi, C. Avendano, and R. O. Duda, "Elevation localization and head-related transfer function analysis at low frequencies," J. Acoust. Soc. Am. **109**(3), 1110–1122 (2001).

[23] W. L. Oberkampf, T. G. Trucano, and C. Hirsch, "Verification, validation, and predictive capability in computational engineering and physics," Appl. Mech. Rev. **57**(5), 345–384 (2004).

[24] S. Bilbao, "Modeling of complex geometries and boundary conditions in finite difference/finite volume time domain room acoustics simulation," IEEE Trans. Audio, Speech, Lang. Process. **21**(7), 1524–1533 (2013).

[25] A. D. Pierce, *Acoustics: An Introduction to Its Physical Principles and Applications* (Acoustical Society of America, Woodbury, New York, 1989).

[26] P. M. Morse and K. U. Ingard, *Theoretical Acoustics* (Princeton University Press, Princeton, NJ, 1986).

[27] K. Kowalczyk and M. van Walstijn, "Formulation of a locally reacting wall in finite difference modelling of acoustic spaces," in *Proceedings of the International Symposium on Room Acoustics (ISRA)*, Seville, Spain (2007), pp. 1–6.

J. Acoust. Soc. Am. **146** (5), November 2019

Prepeliţă *et al.* 3643

[28]C. Webb and S. Bilbao, "Computing room acoustics with CUDA—3d FDTD schemes with boundary losses and viscosity," in *2011 Proceedings of the IEEE International Conference on Acoustics, Speech, and Signal Processing (ICASSP)*, Prague, Czech Republic (2011), pp. 317–320.

[29]J. Sheaffer, M. V. Walstijn, and B. Fazenda, "Physical and numerical constraints in source modeling for finite difference simulation of room acousticsa)," J. Acoust. Soc. Am. **135**(1), 251–261 (2014).

[30]D. Cohen-Or and A. Kaufman, "Fundamentals of surface voxelization," Graph. Models Image Process. **57**(6), 453–461 (1995).

[31]In the present work, the commonly-used term error is chosen in favor of uncertainty despite some inherent practical drawbacks. A further discussion is out of scope—see, e.g., Sec. 2.4 from the text by Oberkampf and Roy (Ref. 20).

[32]R. Holland, "Pitfalls of staircase meshing," IEEE Trans. Electromagn. Compat. **35**(4), 434–439 (1993).

[33]E. Hairer, S. P. Nørsett, and G. Wanner, *Solving Ordinary Differential Equations I: Nonstiff Problems*, 2nd ed. (1993), corr. 3rd ed. (Springer, Heidelberg, London, 2009).

[34]To explore the spatio-temporal dependence of both principal error terms, one can invoke the (multiplicative) separation of variables in Cartesian coordinates and apply the asymptotic expansion of the error independently. For instance, for the 3D wave equation on a Cartesian grid of uniform spacing ΔX, a "separated" solution is of the form $p(\mathbf{r}, t) = p_t(t)p_x(x)p_y(y)p_z(z)$ yielding a second-order simulated solution $\widetilde{p}(\mathbf{r}, t, \Delta T, \Delta X) = \widetilde{p}_t(t, \Delta T)$ $\widetilde{p}_x(x, \Delta X)\widetilde{p}_y(y, \Delta X)$ $\widetilde{p}_z(z, \Delta X) = p(\mathbf{r}, t) + \epsilon_t(t)p_x(x)p_y(y)p_z(z)\Delta T^2 + \epsilon_{\mathbf{r}}(\mathbf{r})$ $p_t(t)\Delta X^2 + \text{HOT}$ where $\epsilon_{\mathbf{r}}(\mathbf{r}) = p_x(x)p_z(z)\epsilon_y(y) + p_x(x)p_y(y)\epsilon_z(z) + p_y(y)$ $p_z(z)\epsilon_x(x)$.

[35]C. J. Roy, "Review of code and solution verification procedures for computational simulation," J. Comput. Phys. **205**(1), 131–156 (2005).

[36]R. May and J. Noye, "The numerical solution of ordinary differential equations: Initial value problems," North-Holland Math. Stud. **83**, 1–94 (1984).

[37]J. Botts and L. Savioja, "Spectral and pseudospectral properties of finite difference models used in audio and room acoustics," IEEE/ACM Trans. Audio, Speech, Lang. Process. **22**(9), 1403–1412 (2014).

[38]J. C. Strikwerda, *Finite Difference Schemes and Partial Differential Equations*, 2nd ed. (SIAM, Philadelphia, PA, 2004).

[39]See equivalent spatial/volumetric arguments in the work by Botts and Savioja (Ref. 57).

[40]J. T. Oden, S. Prudhomme, and L. Demkowicz, "A posteriori error estimation for acoustic wave propagation problems," Arch. Comput. Methods Eng. **12**(4), 343–389 (2005).

[41]J. Botts, A. Bockman, and N. Xiang, "On the selection and implementation of sources for finite-difference methods," in *Proceedings of the 20th International Congress on Acoustics*, Sydney, Australia (2010), pp. 593:1–593:5.

[42]J. Häggblad and O. Runborg, "Accuracy of staircase approximations in finite-difference methods for wave propagation," Numer. Math. **128**(4), 741–771 (2014).

[43]A. C. Cangellaris and D. B. Wright, "Analysis of the numerical error caused by the stair-stepped approximation of a conducting boundary in FDTD simulations of electromagnetic phenomena," IEEE Trans. Antennas Prop. **39**(10), 1518–1525 (1991).

[44]The dependence on frequency stems from, e.g., phase/group delay considerations. For a given angular frequency ω, a phase error will translate in the complex frequency plane as an arc-error of length $\epsilon_{\text{ph}} = \omega\tau_g \pmod{2\pi}$ where τ_g is (for the PRTF solution) the temporal delay error that will behave as $O(\Delta X)/c$. Thus, $\epsilon_{\text{ph}} = \omega O(\Delta X)/c$. Note that, besides the relative orientation of the boundary surface to the grid, the principal error constants for the first-order phase errors also depend on, e.g., the angle of incidence of the incoming (assumed-plane) wave to the (continuous) boundary (Ref. 43).

[45]P. Luizard, M. Otani, J. Botts, L. Savioja, and B. F. Katz, "Comparison of sound field measurements and predictions in coupled volumes between numerical methods and scale model measurements," Proc. Mtgs. Acoust. **19**, 015114 (2013).

[46]S. Bilbao, B. Hamilton, J. Botts, and L. Savioja, "Finite volume time domain room acoustics simulation under general impedance boundary conditions," IEEE/ACM Trans. Audio, Speech, Lang. Process. **24**(1), 161–173 (2016).

[47]The argument can be (roughly) sketched by *fixing* the boundary geometry $\partial\widetilde{\mathcal{D}}(\Delta X) = \partial\widetilde{\mathcal{D}}(\Delta X_i) := \widetilde{\mathcal{D}}_i$, with $\Delta X_i > 0$ and $\widetilde{\mathcal{D}}_i \neq \partial\mathcal{D}$, i.e., there are geometrical errors in the discrete boundary $\widetilde{\mathcal{D}}_i$. Ignoring all other sources of error, for each fixed $\widetilde{\mathcal{D}}_i$ and angular frequency ω, we can perform an asymptotic expansion of the computed solution: $\widetilde{P}_{\mathbf{r}}[\omega] = P_{\mathbf{r},i}[\omega]$ $+ \epsilon_{\mathbf{r},i}[\omega]\Delta X_i^{\min(g,q)} + \text{HOT}$. Wave phenomena dictate that $P_{\mathbf{r},\mathbf{i}}$ is the true/ sought continuous solution $\mathcal{P}_{\mathbf{r}}$ as $\omega/c \to 0$, e.g., we can write an asymptotic expansion in ω for the boundary-induced error $\varepsilon_i[\omega] = P_{\mathbf{r},i}[\omega]$ $- \mathcal{P}_{\mathbf{r}}[\omega]$. $\varepsilon_i[\omega]$ might also propagate in the discretization error terms (e.g., $\epsilon_{\mathbf{r},i}[\omega]$), depending on ω, the topology of the continuous boundary $\partial\mathcal{D}$ and the update scheme. Here, non-physical solutions such as DC are ignored. In practical simulations, due to the (re-)voxelization process, as the grid is refined (i.e., $\Delta X \to 0$), $P_{\mathbf{r},\mathbf{i}}[\omega]$ is expected to change with ΔX by lowering $\varepsilon_i[\omega]$ which in turn will lower the corresponding propagated part in $\epsilon_{\mathbf{r},i}$ (for fixed ω). Moreover, most of such frequencies will not propagate in the update due to the Nyquist-Shannon sampling criterion.

[48]J. Häggblad and B. Engquist, "Consistent modeling of boundaries in acoustic finite-difference time-domain simulations," J. Acoust. Soc. Am. **132**(3), 1303–1310 (2012).

[49]A.-K. Tornberg and B. Engquist, "Consistent boundary conditions for the Yee scheme," J. Comput. Phys. **227**(14), 6922–6943 (2008).

[50]B. Hamilton, "Finite volume perspectives on finite difference schemes and boundary formulations for wave simulation," in *Proceedings of the 17th International Conference on Digital Audio Effects (DAFx-14)*, Erlangen, Germany (2014), pp. 295–302.

[51]K. Salari and P. Knupp, "Code verification by the method of manufactured solutions," SAND2000-1444, Sandia National Labs., Albuquerque, NM; Sandia National Labs., Livermore, CA (2000).

[52]P. M. Morse, "Some aspects of the theory of room acoustics," J. Acoust. Soc. Am. **11**(1), 56–66 (1939).

[53]F. V. Hunt, L. L. Beranek, and D. Y. Maa, "Analysis of sound decay in rectangular rooms," J. Acoust. Soc. Am. **11**(1), 80–94 (1939).

[54]E. W. Cheney and W. A. Light, "Tensor product interpolation," in *A Course in Approximation Theory* (American Mathematical Society, Pacific Grove, CA, 2009), pp. 46–50.

[55]T. I. Laakso, V. Valimaki, M. Karjalainen, and U. K. Laine, "Splitting the unit delay [FIR/all pass filters design]," IEEE Signal Process. Mag. **13**(1), 30–60 (1996).

[56]M. Rosenfeld, "Grid refinement test of time-periodic flows over bluff bodies," Comput. Fluids **23**(5), 693–709 (1994).

[57]J. Botts and L. Savioja, "Effects of sources on time-domain finite difference models," J. Acoust. Soc. Am. **136**(1), 242–247 (2014).

[58]The convergence of such geometric series is satisfied when $\Delta X^2|\mathcal{E}_{X,\text{ref}}[\mathbf{r}_1, \omega] + \mathcal{E}_{T,\text{ref}}[\mathbf{r}_1, \omega]\lambda_{\mathcal{C}}^2/c^2| < |P_{\text{ref}}[\mathbf{r}_1, \omega]|$, where ΔX, $\lambda_{\mathcal{C}}$, and c are all from the free-field simulation. Thus, the series is convergent for a sub-unitary relative (mainly spatial) discretization error of the free-field simulation; alternatively, for ΔX sufficiently small (i.e., solution is within the *asymptotic range*). A small discretization error is obtained for diagonal directions or for lower frequencies $f \ll f_s$ [see the dispersion error analysis for the used (interior) update (Ref. 85) and/or truncation error analysis for the used difference operators]. Thus, if ΔX is not small enough, Eq. (13) could be inaccurate for directions closer to axial directions of the grid, for higher frequencies ω and for far-field (i.e., large $|\mathbf{r}_1|$).

[59]T. Xing and F. Stern, "Factors of safety for Richardson extrapolation," J. Fluids Eng. **132**(6), 061403:1 (2010).

[60]A. V. Oppenheim and C. J. Weinstein, "Effects of finite register length in digital filtering and the fast Fourier transform," Proc. IEEE **60**(8), 957–976 (1972).

[61]L. Trefethen and J. Weideman, "The exponentially convergent trapezoidal rule," SIAM Rev. **56**(3), 385–458 (2014).

[62]F. Stern, R. Wilson, and J. Shao, "Quantitative V&V of CFD simulations and certification of CFD codes," Int. J. Numer. Meth. Fluids **50**(11), 1335–1355 (2006).

[63]D. C. Baird, *Experimentation: An Introduction to Measurement Theory and Experiment Design*, 3rd ed. (Addison-Wesley, Englewood Cliffs, NJ, 1994).

[64]L. Eça and M. Hoekstra, "A procedure for the estimation of the numerical uncertainty of CFD calculations based on grid refinement studies," J. Comput. Phys. **262**, 104–130 (2014).

[65]F. G. Blottner, "Influence of boundary approximations and conditions on finite-difference solutions," J. Comput. Phys. **48**(2), 246–269 (1982).

[66]D. L. Potter, F. G. Blottner, A. R. Black, C. J. Roy, and B. L. Bainbridge, "Visualization of Instrumental Verification Information Details (VIVID): Code development, description, and usage," SAND 2005-1485, Sandia National Laboratories, Albuquerque, New Mexico (2005).

3644   J. Acoust. Soc. Am. **146** (5), November 2019

Prepeliţă *et al.*

[67]G. E. P. Box and P. W. Tidwell, "Transformation of the independent variables," Technometrics **4**(4), 531–550 (1962).

[68]D. C. Montgomery, E. A. Peck, and G. G. Vining, *Introduction to Linear Regression Analysis*, 4th ed. (Wiley-Interscience, Hoboken, NJ, 2006).

[69]J. O. Rawlings, S. G. Pantula, and D. A. Dickey, *Applied Regression Analysis: A Research Tool*, Springer Texts in Statistics, 2nd ed. (Springer-Verlag, New York, 1998).

[70]B. Efron and R. J. Tibshirani, *An Introduction to the Bootstrap* (Chapman and Hall/CRC, New York, NY, 1994).

[71]L. E. Kinsler, F. R. Austin, C. B. Alan, and S. V. James, *Fundamentals of Acoustics*, 4th ed. (Wiley, New York, 2000).

[72]J. O. Smith, *Mathematics of the Discrete Fourier Transform (DFT): With Audio Applications*, 2nd ed. (W3K Publishing, 2007).

[73]E. A. G. Shaw and R. Teranishi, "Sound pressure generated in an external-ear replica and real human ears by a nearby point source," J. Acoust. Soc. Am. **44**(1), 240–249 (1968).

[74]D. W. K. Andrews and M. Buchinsky, "On the number of bootstrap repetitions for BCA confidence intervals," Econom. Theory **18**(4), 962–984 (2002).

[75]W. L. Oberkampf and T. G. Trucano, "Verification and validation in computational fluid dynamics," Prog. Aerosp. Sci. **38**(3), 209–272 (2002).

[76]P. Mokhtari, H. Takemoto, R. Nishimura, and H. Kato, "Vertical normal modes of human ears: Individual variation and frequency estimation from pinna anthropometry," J. Acoust. Soc. Am. **140**(2), 814–831 (2016).

[77]J. Saarelma and L. Savioja, "An open source finite difference time-domain solver for room acoustics using Graphics Processing Units," in *Proceedings of the Forum Acusticum*, European Acoustics Association, Krakow, Poland (2014), pp. 1–6.

[78]"CUDA-Aware OpenMPI distribution" (2018), https://www.open-mpi.org/faq/?category=runcuda (Last viewed March 10, 2018).

[79]E. Jones, T. Oliphant, and P. Peterson, "${$scipy$}$: Open source scientific tools for ${$python$}$" (2014), url: http://www.scipy.org/ (Last accessed February 1, 2019).

[80]S. V. d. Walt, S. C. Colbert, and G. Varoquaux, "The NumPy array: A structure for efficient numerical computation," Comput. Sci. Eng. **13**(2), 22–30 (2011).

[81]J. Fox and S. Weisberg, *An R Companion to Applied Regression*, 2nd ed. (SAGE Publications, Inc., Thousand Oaks, CA, 2010).

[82]S. Seabold and J. Perktold, "Statsmodels: Econometric and statistical modeling with python," in Proceedings of the 9th Python in Science Conference, SciPy Society, Austin, TX (2010), pp. 57–61.

[83]G. Gopalakrishnan, R. M. Kirby, S. Siegel, R. Thakur, W. Gropp, E. Lusk, B. R. De Supinski, M. Schulz, and G. Bronevetsky, "Formal analysis of MPI-based parallel programs," Commun. ACM **54**(12), 82–91 (2011).

[84]B. Gustafsson, H.-O. Kreiss, and J. Oliger, *Time-Dependent Problems and Difference Methods*, 2nd ed. (Wiley, Hoboken, NJ, 2013).

[85]K. Kowalczyk and M. van Walstijn, "Room acoustics simulation using 3-D compact explicit FDTD schemes," IEEE Trans. Audio, Speech, Lang. Process. **19**(1), 34–46 (2011).

J. Acoust. Soc. Am. **146** (5), November 2019

Prepeliţă *et al.* 3645